Realization of Complex III-V Nanoscale Heterostructures

Gorji, Sepideh

2014

Realization of Complex III-V Nanoscale Heterostructures

Sepideh Gorji Ghalamestani
Doctoral thesis
2014

LUND
UNIVERSITY

DOCTORAL DISSERTATION
by due permission of the Faculty of Engineering, Lund University, Sweden.

To be defended at Rydbergsalen, Sölvegatan 14, Lund. Date 23th May and time 9:30.
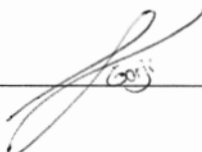
Faculty opponent

Dr. Jean-Christophe Harmand

Laboratoire de Photonique et de Nanostructures (LPN-CNRS)

Organization	Document name
LUND UNIVERSITY	DOCTORAL DISSERTATION
	Date of issue 2014-05-23
Author Sepideh Gorji Ghalamestani	Sponsoring organization

Title and subtitle

Realization of Complex III-V Nanoscale Heterostructures

Abstract

Low-dimensional III-V semiconductor nanoscale structures grown by epitaxial processes have emerged as a new class of materials with great promise for various device applications. This thesis describes explorations into the heteroepitaxial growth of III-V semiconductor materials in combination with other III-V materials and in combination with the commonly used Si material, in both thin layer and nanowire geometries. Understanding the heteroepitaxial growth of III-V semiconductor nanoscale structures, and understanding the thermodynamic and kinetic processes involved in the growth of these structures, provides deeper insight into their formation properties. Such understanding also enables highly controlled fabrication of high quality crystal nanostructures composed of these materials, which are of great importance for both advanced physics studies and the next generation of devices.

This thesis describes work to explore and understand the heteroepitaxial growth of several promising III-V semiconductor materials, including InAs, GaAs, InP, InSb, and GaSb. The properties of these materials, such as their mobility and their direct band gap, are superior to those of the widely used Si material. The materials have been grown using metalorganic vapor phase epitaxy and molecular beam epitaxy.

This thesis describes also the successful epitaxial growth of high quality and thin InAs and GaSb layers on Si substrates, despite the large lattice mismatch between these. It describes also studies of several complex III-V nanowire heterostructures in both axial and radial geometries, such as single axial and double axial InSb-GaSb nanowires in both directions. Moreover, investigation of the radial heteroepitaxial growth of Au-seeded InAs-InP and self-seeded GaAs-$GaAs_xSb_{1-x}$ nanowires, which indicated important roles of crystal quality and various surface energies, is described.

The combination of two binary materials into a ternary nanowire, apart from scalability, offers the possibility to precisely tune the band gap and carrier mobility for specific applications. Hence, this thesis describes studies into the formation of GaAs-$GaAs_xSb_{1-x}$ core-shell nanowires with tuned compositions and into the epitaxial growth of $Ga_xIn_{1-x}Sb$ ternary nanowires for the first time.

Key words III-V semiconductor, nanowire, heterostructures, MBE, MOVPE

Classification system and/or index terms (if any)

Supplementary bibliographical information	Language English

ISSN and key title	ISBN 978-91-7473-991-6

Recipient's notes	Number of pages 168	Price
	Security classification	

I, the undersigned, being the copyright owner of the abstract of the above-mentioned dissertation, hereby grant to all reference sources permission to publish and disseminate the abstract of the above-mentioned dissertation.

Signature _____ Date 2014-04-09

Realization of Complex III-V Nanoscale Heterostructures

Sepideh Gorji Ghalamestani

Doctoral thesis
2014

Cover: Scanning electron micrograph of Au-seeded InAs-InSb-GaInSb nanowires grown under conditions leading to high radial overgrowth and low aspect ratio, yielding a diamond-shape morphology.

Intertek ™

MILJÖMÄRKT 341903

REPA
En del av Förpacknings- och
Tidningsinsamlingen (FTI)

Abstract

Low-dimensional III-V semiconductor nanoscale structures grown by epitaxial processes have emerged as a new class of materials with great promise for various device applications. This thesis describes explorations into the heteroepitaxial growth of III-V semiconductor materials in combination with other III-V materials and in combination with the commonly used Si material, in both thin layer and nanowire geometries. Understanding the heteroepitaxial growth of III-V semiconductor nanoscale structures, and understanding the thermodynamic and kinetic processes involved in the growth of these structures, provides deeper insight into their formation properties. Such understanding also enables highly controlled fabrication of high quality crystal nanostructures composed of these materials, which are of great importance for both advanced physics studies and the next generation of devices.

This thesis describes work to explore and understand the heteroepitaxial growth of several promising III-V semiconductor materials, including InAs, GaAs, InP, InSb, and GaSb. The properties of these materials, such as their mobility and their direct band gap, are superior to those of the widely used Si material. The materials have been grown using metalorganic vapor phase epitaxy and molecular beam epitaxy.

This thesis describes also the successful epitaxial growth of high quality and thin InAs and GaSb layers on Si substrates, despite the large lattice mismatch between these. It describes also studies of several complex III-V nanowire heterostructures in both axial and radial geometries, such as single axial and double axial InSb-GaSb nanowires in both directions. Moreover, investigation of the radial heteroepitaxial growth of Au-seeded InAs-InP and self-seeded GaAs-GaAs$_x$Sb$_{1-x}$ nanowires, which indicated important roles of crystal quality and various surface energies, is described.

The combination of two binary materials into a ternary nanowire, apart from scalability, offers the possibility to precisely tune the band gap and carrier mobility for specific applications. Hence, this thesis describes studies into the formation of GaAs-GaAs$_x$Sb$_{1-x}$ core-shell nanowires with tuned compositions and into the epitaxial growth of Ga$_x$In$_{1-x}$Sb ternary nanowires for the first time.

Contents

List of Papers

This thesis is based on the following papers:

I. High quality InAs and GaSb thin layers grown on Si (111)

S. Gorji Ghalamestani, M. Berg, K.A. Dick, L-E. Wernersson

J. Cryst. Growth. 2011. **332**: pp. 12-16.

I grew the layers, performed SEM, AFM, and XRD characterizations and was responsible for writing the paper.

II. Uniform and position-controlled InAs nanowires on 2" Si substrates for transistor applications

S. Gorji Ghalamestani, S. Johansson, B.M. Borg, E. Lind, K.A. Dick, L-E. Wernersson

Nanotechnology. 2012. **23**: pp. 015302.

I grew the layers and nanowires, performed SEM and AFM characterizations, coordinated data analysis, and wrote most of the paper.

III. Realization of single and double axial InSb-GaSb heterostructure nanowires

S. Gorji Ghalamestani, M. Ek, K.A. Dick

Phys. Status Solidi RRL. 2014. **8**: pp. 269-273.

I initiated the study, designed the experiments, grew the nanowires, performed SEM characterization, coordinated data analysis, and was responsible for writing the paper.

IV. Growth of InAs/InP core-shell nanowires with various pure crystal structures

S. Gorji Ghalamestani, M. Heurlin, L-E. Wernersson, S. Lehmann, K.A. Dick

Nanotechnology. 2012. **23**: pp. 285601.

I partly designed the experiments, grew the nanowires, performed SEM characterization, coordinated data analysis, and was responsible for writing the paper.

V. Self-catalyzed MBE grown GaAs/GaAs$_x$Sb$_{1-x}$ core-shell nanowires in ZB and WZ crystal structures

S. Gorji Ghalamestani, A.M. Munshi, D.L. Dheeraj, B-O. Fimland, H. Weman, K.A. Dick

Nanotechnology. 2013. **24**: pp. 405601.

I designed the experiments together with colleagues at NTNU, participated in the growth of nanowires, performed part of SEM characterization, coordinated data analysis, and was responsible for writing the paper.

VI. Demonstration of Defect-Free and Composition Tunable Ga$_x$In$_{1-x}$Sb Nanowires

S. Gorji Ghalamestani, M. Ek, B. Ganjipour, C. Thelander, J. Johansson, P. Caroff, K.A. Dick

Nano Lett. 2012. **12**: pp. 4914-4919.

I planned the project, designed the experiments, grew the nanowires, performed SEM characterization, coordinated data analysis, and was responsible for writing the paper.

VII. Morphology and composition controlled Ga$_x$In$_{1-x}$Sb nanowires: Understanding ternary antimonide growth

S. Gorji Ghalamestani, M. Ek, M. Ghasemi, P. Caroff, J. Johansson, K.A. Dick

Nanoscale. 2014. **6**: pp. 1086-1092.

I planned the project, designed the experiments, grew the nanowires, performed SEM characterization, coordinated data analysis, and was responsible for writing the paper.

Papers and patent not included in this thesis:

I. Highly controlled InAs nanowires on Si (111) wafers by MOVPE

S. Gorji Ghalamestani, S. Johansson, B.M. Borg, K.A. Dick, L-E. Wernersson

Phys. Status Solidi C. 2012. **9**: pp. 206-209.

II. Temperature and annealing effects on InAs nanowire MOSFETs

S. Johansson, **S. Gorji Ghalamestani**, M. Borg, E. Lind, L-E. Wernersson

Microelectron. Eng. 2011. **88**: pp. 1105-1108.

III. RF Characterization of Vertical InAs Nanowire Wrap-Gate Transistors Integrated on Si Substrates

S. Johansson, M. Egard, **S. Gorji Ghalamestani**, B.M. Borg, M. Berg, L-E. Wernersson, E. Lind

IEEE Trans. Microwave Theory Tech. 2011. **59**: pp. 2733-2738.

IV. High frequency vertical InAs nanowire MOSFETs integrated on Si substrates

S. Johansson, **S. Gorji Ghalamestani**, M. Egard, B.M. Borg, M. Berg, L-E. Wernersson, E. Lind

Phys. Status Solidi C. 2012. **9**: pp. 350-353.

V. Patent application

Substrate comprising Si-base and InAs layer

L-E. Wernersson and **S. Gorji Ghalamestani**

Patent Cooperation Treaty application PCT/SE2012/050447

US provisional patent: No. 14/113,438

US publication no.: US 2014/0048851 A1

Europe application number: EP 12729250.6

Abbreviations

1D	One-dimensional
2D	Two-dimensional
3D	Three-dimensional
AFM	Atomic force microscope/microscopy
APD	Anti-phase domain
AsH_3	Arsine
bcc	Body-centered cubic
BSE	Backscattered electron
CBE	Chemical beam epitaxy
CMOS	Complementary metal-oxide-semiconductor
fcc	Face-centered cubic
FEG	Field emission gun
FET	Field-effect transistor
HAADF	High angle annular dark field
hcp	Hexagonal closed packed
HRTEM	High resolution transmission electron microscope/microscopy
LED	Light-emitting diode
MBE	Molecular beam epitaxy
MEMS	Micro-electromechanical system
MFC	Mass flow controller
MOCVD	Metalorganic chemical vapor deposition
MOVPE	Metalorganic vapor phase epitaxy
nm	Nanometer (10^{-9} meters)
NEMS	Nano-electromechanical system

PhAs	Phenylarsine
PH$_3$	Phosphine
QD	Quantum dot
RHEED	Reflection high-energy electron diffraction
RMS	Root mean square
RSM	Regular solution model
SAE	Selective area epitaxy
SbH$_3$	Stibine
SE	Secondary electron
SEM	Scanning electron microscope/microscopy
SK	Stranski-Krastanov
SPM	Scanning probe microscope/microscopy
STEM	Scanning transmission electron microscope/microscopy
TBAs	Tertiary-butyl arsine
TBP	Tertiary-butyl phosphine
TEGa	Triethylgallium
TESb	Triethylantimony
TEM	Transmission electron microscope/microscopy
TM	Tapping mode
TMGa	Trimethylgallium
TMIn	Trimethylindium
TMSb	Trimethylantimony
TPB	Triple-phase boundary
TSL	Twin-plane superlattice
UHV	Ultra-high vacuum (pressure lower than 10^{-9} mbar)
VLS	Vapor-liquid-solid
VS	Vapor-solid
VSS	Vapor-solid-solid
WZ	Wurtzite
XEDS	X-ray energy dispersive spectrometry

14

XRD	X-ray diffraction
ZB	Zinc blende
μm	Micrometer (10^{-6} meters)
Å	Ångström (10^{-10} meters)

Symbols

A	Area
a	Lattice constant
D	Diameter
d	Atomic plane distance
E	Electron beam energy
E_c	Conduction band minimum energy
E_g	Band gap
E_v	Valence band maximum energy
F	Force
G	Gibbs free energy
H	Enthalpy
h	Height
k	Spring constant
k_B	Boltzmann constant (1.38065×10^{-23} J/K)
P	Perimeter
p	Vapor pressure
r	Radius
S	Entropy
T	Temperature
V	Volume
X	Cantilever deflection
Z	Element atomic number
β	Contact angle
γ	Surface energy

ε	Strain
θ	Incident beam angle
λ	Wavelength
μ	Chemical potential
$\Delta\mu$	Supersaturation
Ω	Atomic volume
Ω_i	Interaction parameter

1. Introduction

Nanoscience and nanotechnology have emerged in recent decades as key fields in various scientific fields such as chemistry, biology and physics. In general, nanoscience and nanotechnology aim to understand the properties of structures at the nanometer scale (nanoscale) in at least one dimension, and to design and construct technological devices at this scale [1].

Nanoscale objects are fabricated using either "top-down" or "bottom-up" approaches. Bottom-up construction is used in organic and supramolecular chemistry, through reactions and self-assembly. Molecular biology also studies the association of biological molecules to generate nanobiological structures with certain functions [2]. Both top-down and bottom-up approaches are used in physics for the miniaturization of "continuous matter". The bottom-up approach manipulates individual atoms and molecules to produce materials at nanoscale, whereas the top-down approach relies on downscaling structures in industrial technology by sophisticated techniques. Micro- and nano-electromechanical systems (MEMS and NEMS) are examples of such downscaling concepts with great potential for various applications such as sensors [3, 4].

As the dimensions of a material decrease, interesting geometrical and physical effects appear. The surface-to-volume ratio, for example, becomes extremely important, as a greater proportion of the material comes in contact with the environment and a greater proportion of bonds become "dangling bonds". These increases influence the material's stability and its chemical properties. The high surface-to-volume ratio may also affect the reactivity of nanoscale materials in structures such as nanoparticles [5]. The physical properties of nanoscale materials are also different from those of macroscale materials, and different aspects of physical laws (quantum effects) must be considered when studying nanoscale materials. Electrons can tunnel through quantum barriers in nanoscale materials, for example, that they cannot get through in macroscale materials, where classical physics applies.

Understanding the properties of nanoscale objects requires results obtained from many analytical techniques with high spatial resolution to determine and quantify the atomic structure and composition of the objects. Continuous developments in the synthesis of nanoscale structures and advances in analytical techniques have led to great advances in both nanoscience and nanotechnology. Nanoscience and nanotechnology are now employed in many applications, such as nanoelectronics,

sensors, data storage, energy storage (solar cells and fuel cells) and coatings. The ultimate goal of nanoscience and nanotechnology is to build on the significant advances made in these fields, and to understand and fabricate nanoscale structures with atomic precision for industrial applications. Accomplishing this goal requires a greater understanding of the formation properties of nanoscale structures and tighter control of their fabrication processes.

1.1. III-V semiconductor nanostructures

Many studies in nanoscience and nanotechnology have been devoted to semiconducting materials and their applications. Semiconducting materials are an important class of materials with outstanding properties, used in many applications. The term "semiconductor" refers to a member of a group of materials with electrical conductivities that lie between those of metals and insulators. In general, the electrons inside a material are allowed to occupy certain energy levels known as "bands". The term "valence band" denotes the upper energy band filled by electrons, where the maximum level is denoted E_v. The term "Fermi" level denotes the chemical potential of the electrons in the semiconductor material at 0 K. The allowed energy band above the Fermi level is known as the "conduction" band, and its minimum is denoted E_c. The separation between E_v and E_c is known as the "band gap", E_g (where $E_c - E_v = E_g$). Materials can be classified on the basis of their band gap into three classes, known as "metals", "semiconductors" and "insulators", where metals have negligibly small band gaps, and insulators have band gaps so large that it is unfeasible that an electron can cross. In general, a semiconductor material has a small band gap, and applying an electric field, light or thermal energy can excite an electron from the valence band to the conduction band.

The band gap of a semiconductor material is either "direct" or "indirect". If the minimum energy state of the conduction band and the maximum energy state of the valence band are in the same momentum, the semiconductor material has a direct band gap. Otherwise, the semiconductor material has an indirect band gap. Direct band gap materials are particularly interesting for optical applications. Photons (with energies greater than the band gap) can, for example, excite electrons from the maximum energy state of the valence band to the minimum energy state of the conduction band, leaving holes in the valence band. The excited electrons then for instance recombine with holes to create photons.

Si (a Group IV element) is the most dominant semiconductor material and has been extensively used in various electronic applications, due to its abundance in nature and beneficial oxide form. However, Si is an indirect band gap semiconductor material and is therefore not suitable for optical applications.
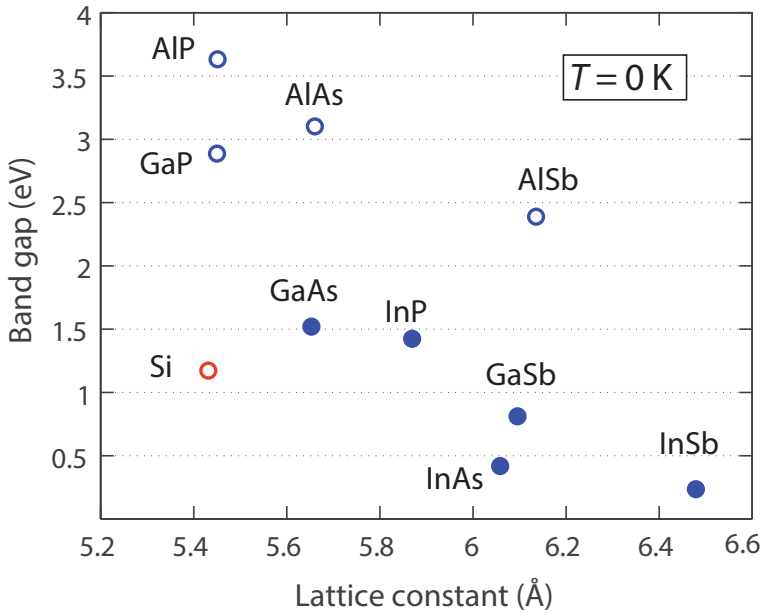
Figure 1.1 The relationship between band gap and lattice constant for several III-V semiconductor materials and Si (Group IV) at 0 K. The open data points represent indirect band gap materials, the filled data points direct band gap materials [6].

Other novel materials, such as carbon-nanotube and III-V compounds, are highly required, in order to be able to continue the downscaling trend in nanoelectronics while at the same time improving the performance of devices [7].

In general, III-V semiconductor materials (compounds of Group III and Group V elements) have more interesting properties than Group IV elements. Figure 1.1 shows the relationship between the band gap and the interatomic distance, known as the "lattice constant", of several III-V semiconductor materials (blue data points) together with Si (red data point).

Most of the III-V semiconductor materials considered have direct band gaps (filled data points). Additionally, most of the III-V materials have higher carrier mobility than Si, making them suitable for high-frequency electronic devices. InAs and GaSb, for example, have electron and hole bulk mobilities of 35,000 $cm^2V^{-1}s^{-1}$ and 5,600 $cm^2V^{-1}s^{-1}$, respectively, at 77 K [8].

Introduction

InSb has the highest bulk electron mobility of III-V semiconductor materials, 77,000 $cm^2V^{-1}s^{-1}$ (at 300 K), and the smallest band gap [9]. It should be noted that the properties of the semiconductor materials (such as carrier concentration, mobility, and band gap) can be modified by adding dopants. It has been shown that the crystal structure of a semiconductor material also affects the magnitude of its band gap [10-12].

III-V semiconductor nanostructures can be synthesized with reduced dimensions, and include quasi two-dimensional (2D) nanostructures (thin layers), one-dimensional (1D) nanostructures (nanowires), and zero-dimensional nanostructures (quantum dots (QD)).

Thin layer (2D) nanostructures have been extensively investigated in recent decades. These studies have included their formation properties and their use in various types of application, such as multijunction solar cells [13], light-emitting diodes (LED) [14] and field-effect transistors (FET) [15]. In particular, combinations of high mobility III-V semiconductor thin layers with the well-established Si technology is a promising approach to continue the common scaling trend in nanoelectronics. Currently, high quality thin layers are used in several applications, such as multijunction solar cells. However, combining materials with dissimilar unit cell spacings, known as "lattice mismatch", introduces fundamental limitations. It is challenging to create high quality thin layers of lattice-mismatched materials systems. In fact, reducing the material dimension is an attractive approach to avoid such fundamental issues, and this suggests that the use of 1D geometry is a promising approach.

Nanowire geometry (1D) offers additional interesting possibilities, compared to the thin layers. First, nanowires serve as a platform to understand the fundamental properties of materials at the nanoscale size, including combinations of lattice-mismatched material systems. Second, nanowires have served as building blocks for various device applications such as solar cells [16, 17], nanoelectronic devices [18, 19], optoelectronic devices [20, 21] and quantum devices [22-25]. Additionally, the synthesis of the III-V semiconductor materials in the form of high quality nanowires with scalable dimensions is an alternative path for the further downscaling of semiconductor devices [26].

As stated above, nanowire geometry allows defect-free lattice-mismatched material systems to be combined on top of each other, as the strain induced from the lattice mismatch is released by expansion or contraction of materials near the interface (not possible in 2D). Moreover, nanowire geometry enables the nanowire surface to be passivised with other material systems. Electron/hole mobility, for example, is often lower in nanowire geometry than it is in bulk material, due to surface scattering. It is possible, however, to passivate/protect the surface of high mobility nanowires with a material that has a wider band gap. As an example, it has been reported that passivating InAs nanowire surface with a thin InP layer enhances their transport

properties [27, 28]. The possibility of passivating nanowires makes them even more interesting candidates for several electronic and optoelectronic applications when high surface-to-volume ratios are needed [29, 30]. Finally, the combination of two binary materials into a ternary nanowire allows precise engineering of its physical properties, such as its composition and band gap.

1.2. Thesis synopsis

This thesis focuses on the synthesis properties of combined semiconductor nanostructures in thin layer and nanowire geometries. In particular, it describes investigations into the combination of several interesting III-V semiconductor materials, including InAs, GaAs, InP, InSb, GaSb. Furthermore, studies of the combination of some III-V semiconductor nanostructures with Si substrates are also discussed.

Chapter 2 introduces the crystal structure of III-V semiconductor materials in layer and nanowire geometries. One method of synthesis of III-V semiconductor materials, known as "epitaxy", is described, and two epitaxial techniques are explained. The key thermodynamic and kinetic parameters involved in an epitaxial process are addressed.

Chapter 3 introduces the characterization techniques used during the work described in this thesis to study the properties, such as morphology, composition and crystal structure, of the epitaxially grown nanostructures.

Chapter 4 describes the fundamental principles of layer growth, and presents the main challenges of III-V growth on Group IV substrates. The results of GaSb and InAs layer growth on Si substrates and the layer growth of GaSb on epitaxially grown InAs thin layers on Si substrates are presented.

Chapter 5 describes the fundamental principles of nanowire growth, and describes the thermodynamic and kinetic aspects of the processes involved. The challenges of antimonide-based nanowire growth are described, and this system is compared with the more common arsenide-based and phosphide-based systems. Three complex nanowire heterostructures are introduced and discussed, followed by examples of each.

Finally, Chapter 6 summarizes the results presented in this thesis, and suggests future work in this area.

2. Crystal growth

Semiconductor materials are solid crystals in which atoms are positioned in an ordered fashion, unlike amorphous materials, in which atoms are randomly positioned. A unit cell of the crystal is the smallest building block that can form the crystal. Common types of unit cell are cubic, body-centered cubic (bcc), face-centered cubic (fcc) and hexagonal closed packed (hcp) lattices. The equilibrium bulk crystal structure of most III-V semiconductor materials is the zinc blende structure (ZB), which is an fcc structure with two different atoms at each basis point. The nitride-based materials are an exception to this: they have the wurtzite (WZ) structure.

Unlike bulk III-V materials, III-V nanowires form several crystal structures, including, ZB, WZ and mixed structures. This unique property allows for the formation of materials with crystal structures that are not stable in the bulk form. Hence, apart from the size scalability, crystal structure tuning adds another degree of freedom to nanowires.

2.1. Crystal structure

The atoms in crystals are packed in a particular way. We describe in this section the crystallographic structure of nanowires grown in the $[\bar{1}\bar{1}\bar{1}]$ direction (see Section 5.1), since $<\bar{1}\bar{1}\bar{1}>$ is the common direction of the nanowire growth.

The ZB crystal structure is an fcc structure and WZ is an hcp. The {111} planes in the fcc lattice, which are equivalent to the {0001} planes in the hcp lattice, are "close-packed", since the atomic distances in these planes are the shortest within the structure. Figure 2.1 illustrates the WZ and ZB atomic structures, showing what are known as "stacking sequences", in the close-packed plane directions.

The difference between the ZB and WZ crystal structures can be explained through their different stacking sequences. Each alternating bilayer (composed of a monolayer of Group III and a monolayer of Group V atoms) is identical in the WZ structure. Its atomic sequence thus is ABAB…. The ZB crystal structure, in contrast, has three layers with different orientations and the stacking sequence is thus ABCABC….
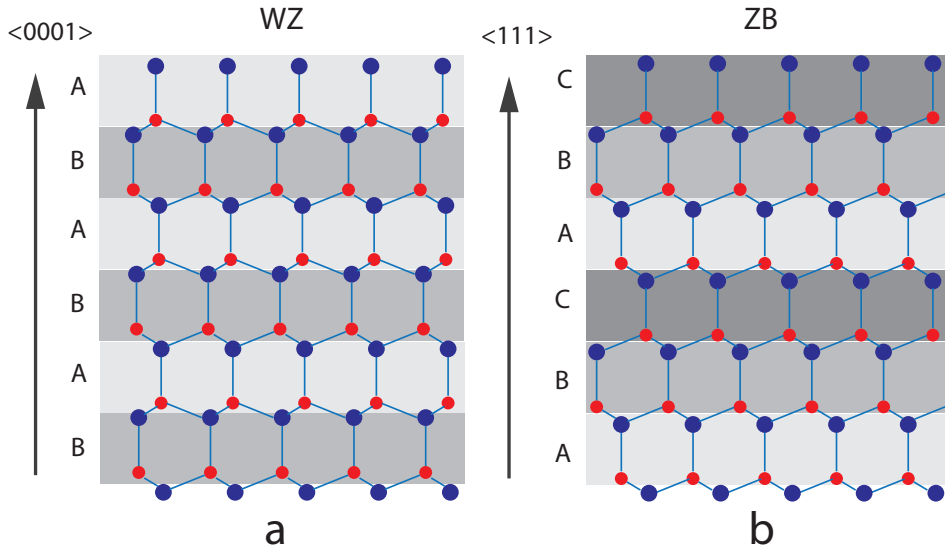
Figure 2.1 (a) WZ and (b) ZB crystal structures in the close-packed planes, demonstrating the ABAB… and ABCABC… stacking sequences, respectively.

Misplacement of a single bilayer in the WZ structure creates a stacking fault, such as ABA**B**|**C**BCB…, where the stacking fault lies between **B** and **C** planes, to create a unit of the ZB structure (A**BC**). Misplacement of a single bilayer in the ZB structure creates a twin plane, such as ABC**A**CBA…, where the **A** plane is a mirror plane. Formation of further twin planes creates WZ segments within the ZB crystal structure.

The atomic structures described above are examples of mixed WZ and ZB crystal structures, and these occur often during nanowire growth. Controlling the crystal structure of the nanowires has been the subject of many studies [31-35].

There are other differences between the WZ and ZB crystal structures. The neighboring atoms to any particular atom can be divided into four groups, based on their distances from it. The atoms at the closest distance are the "1st nearest neighbors". The next closest are the "2nd nearest neighbors" and so on. The 1st and 2nd nearest neighbors distances are the same in the WZ and ZB structures, as are the numbers of each type of neighbor. The 3rd nearest neighbor atom in WZ is, however, closer than in the ZB crystal structure.

The two types of atom that make up a bilayer in III-V semiconductor materials are different, and a charge polarity, known as "ionicity", may be present between the Group III and Group V atoms, depending on their difference in electronegativity [36, 37]. It has been suggested that the ionicity acts as a driving force for the formation of

certain crystal structures, so that high ionicity favors WZ, and low ionicity ZB. The antimonide-based nanowires, for example, have a low ionicity, and almost always grow in the ZB crystal structure; some authors have attributed the formation of the ZB crystal structure in antimonides to their low ionicity [38-41].

It should be mentioned that depending on the atomic arrangement, different crystallographic planes have different properties such as surface energy and anisotropy. The surface energy depends not only on the crystal plane, but also on the chemical composition, surface morphology (i.e. roughness) and atomic reconstruction [42]. The anisotropic nature of the different atomic planes also affects their surface energy and thus their growth rate. Some examples of different growth rates at different atomic planes (nanowire side facets) are presented in Section 5.3.2.

2.2. Epitaxy

"Epitaxy" is the ordered deposition of a material onto a monocrystalline substrate, and it is often used to form III-V semiconductor nanostructures. "Homoepitaxy" is the term used when the epitaxial layer and the underlying substrate are of the same type, "heteroepitaxy" when they are different. Epitaxy is a common bottom-up technique used for the growth of high quality monocrystalline materials.

The epitaxial growth of semiconductor materials can be achieved by several techniques such as molecular beam epitaxy (MBE), metalorganic vapor phase epitaxy (MOVPE), and chemical beam epitaxy (CBE). The MOVPE system uses metalorganic vapor precursors in a carrier gas, and requires chains of chemical reactions, including pyrolysis of the individual precursors, to form the desired elements, followed by surface reactions. MBE uses molecular beams in an ultra-high vacuum (UHV) environment, and fewer chemical reactions are involved.

CBE is essentially the MOVPE process in an UHV system, and can be considered as a combination of the MOVPE and MBE techniques. Each of these techniques has some strengths and weaknesses. MOVPE, however, is the most flexible epitaxial growth technology, and it has been successfully used for large-scale applications [43-45].

2.2.1. Metalorganic vapor phase epitaxy

Most of the specimens examined during the work described in this thesis were grown in a cold-wall and low-pressure (100 mbar) MOVPE system (Aixtron 200/4). Growth takes place in the reactor, which is the main part of the MOVPE system. The MOVPE system used for this work had a horizontal reactor designed for three 2" wafers or one 4" wafer. The substrate was placed on a graphite surface known as the

"susceptor", heated from below by infrared lamps. The maximum temperature that could be achieved in the reactor was 750 °C. Figure 2.2 shows the structure of a MOVPE system. Hydrogen with a total flow rate of 13 l/min was used as a carrier gas during the growth to transfer metalorganics (mainly of Group III elements) and hydrides (of Group V elements) to the reaction chamber. During and after the epitaxial process, un-reacted and waste materials were sent to the exhaust line and burned safely.

Each material flow is controlled by a mass flow controller (MFC). Most metalorganic Group III materials are liquids (the indium source trimethylindium (TMIn) is a solid). The metalorganic sources are kept in what are known as "bubblers" to maintain a constant temperature, and their rates of flow are controlled by the rate of hydrogen flow through the bubblers. One hydrogen pipe enters the liquid and a second collects the precursors in the vapor phase. Group V precursors, in contrast, are mainly in the gaseous hydride form, except the metalorganic antimonide source trimethylantimony (TMSb). The epitaxial growth processes are controlled by several parameters, such as temperature and the molar fractions of reactants. As an example, GaAs can be grown from trimethylgallium (TMGa) and arsine (AsH$_3$) with the overall reaction (Equation 2.1):

$$Ga(CH_3)_3 + AsH_3 \rightarrow GaAs + 3\ CH_4 \qquad (2.1)$$
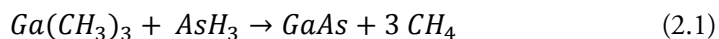
Incomplete pyrolysis of the metalorganic precursors can lead to carbon contaminations in the growing material, which could act as a dopant. It is difficult to control the incorporation of carbon into the growing material, and carbon contamination of the grown material is the main disadvantage of the MOVPE system. MOVPE, however, is the most flexible epitaxial growth technology, and can be used for large-scale systems.
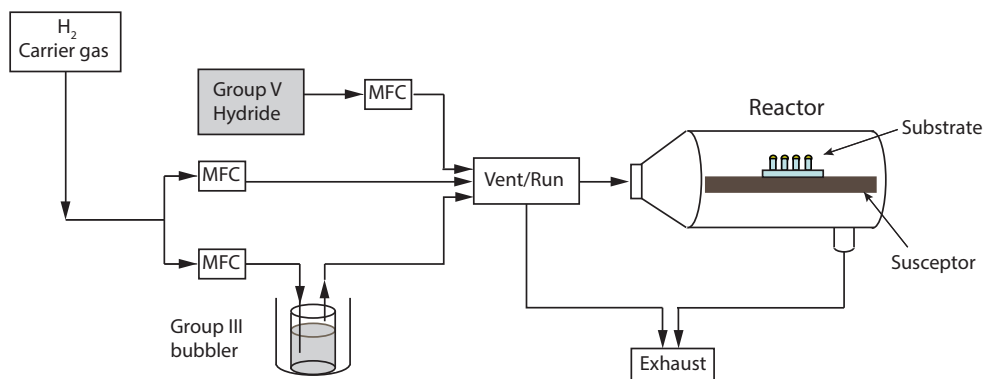

Figure 2.2 A MOVPE system in which hydrogen is used as the carrier gas. Metalorganic sources are kept in the bubblers and their flows are controlled by MFCs. The epitaxial growth process occurs inside the reactor and the waste materials are transported to the exhaust pipe.

2.2.2. Molecular beam epitaxy

MBE is another versatile epitaxial growth technique used to obtain high quality samples [46, 47]. The principle of MBE is simpler than that of MOVPE. GaAs growth by MBE occurs as described by Equation 2.2.

$$Ga + \frac{1}{2}As_4 \rightarrow GaAs + \frac{1}{2}As_2 \tag{2.2}$$
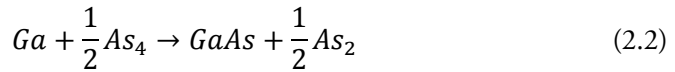
The source materials are placed in solid form into effusion cells, where they are heated to produce atoms or clusters of atoms. The chamber is kept under UHV conditions, and this ensures that the evaporated materials have long mean free paths, enabling them to reach the substrate and become incorporated into the growing layer (or nanowire). The long mean free path also prevents homogeneous reactions in the gas phase. The flux of the atoms (or clusters of atoms) is adjusted by controlling the temperature of the effusion cell, and it can be completely closed using a shutter located in front of the cell.

One main advantage of MBE over MOVPE is the high purity of the material that is grown (no carbon contamination). Another advantage is the possibility of installing equipment for *in situ* characterization techniques such as reflection high-energy electron diffraction (RHEED). *In situ* monitoring is possible also in MOVPE, but the techniques available are less universally useful than RHEED. The disadvantages of MBE are its low throughput and the need for UHV conditions, which make it expensive.
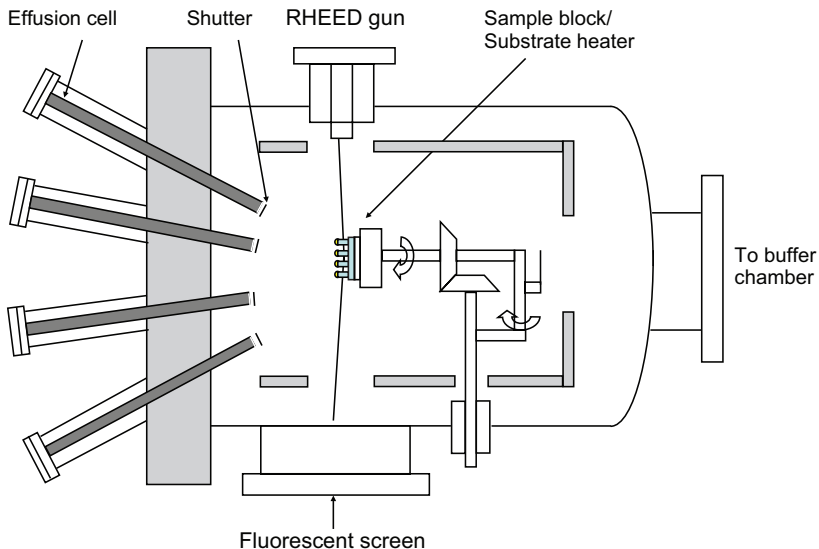

Figure 2.3 An MBE reactor [Courtesy of D.L. Dheeraj]. The system is in UHV conditions, which enables the RHEED technique to be used to monitor the surface reconstruction.

Crystal growth

Some samples were grown in a Varian Gen II Modular MBE system, located in the MBE lab at NTNU, Norway. Figure 2.3 shows the chamber of this system. It is equipped with ion pumps and a cooling system to achieve UHV conditions. The substrate is located in the center and is equidistant from the effusion cells, in spherical geometry. The system is equipped with various cells, such as As, Sb and Ga cells.

The two techniques described above differ, but the principle of both techniques is similar, and the epitaxial growth is governed by two key factors: thermodynamics and kinetics. Thermodynamics determines the direction of a reaction, and kinetics determines the rate of the reaction.

2.3. Thermodynamics

Thermodynamics is the driving force of the epitaxial growth process, and it causes the precursor molecules to react and form the epitaxial structures. This section discusses the thermodynamic aspects of vapor-phase epitaxy, and describes in detail the differences between layer growth and nanowire growth.

Thermodynamics deals with energy changes in a system. If we consider a simple system composed of only one component, where v indicates the reactant in the vapor phase and s indicates the product in the solid phase, equilibrium is reached when the chemical potential of the reactant (μ_v) equals the chemical potential of the product (μ_s):

$$R_v \leftrightarrow P_s \; \rightarrow \; \mu_v = \mu_s \; \rightarrow \; \Delta\mu = \mu_v - \mu_s = 0 \qquad (2.3)$$

where R_v is reactant in vapor phase and P_s is product is solid phase. In other words, in the equilibrium condition, there is no chemical potential difference between the reactant and product ($\Delta\mu = 0$). In a non-equilibrium condition, the chemical potential difference is not zero (either $\Delta\mu > 0$ or $\Delta\mu < 0$). For positive chemical potential difference ($\Delta\mu > 0$), condensation occurs, while for negative chemical potential difference ($\Delta\mu < 0$) evaporation occurs.

The chemical potentials of the reactants are increased in vapor-phase epitaxy growth by supplying more material [43]. Epitaxial growth is an example of a non-equilibrium condition in which $\Delta\mu$ is positive. As a result, thermodynamics acts as the driving force for the reaction to proceed, and to lower the energy of the system. The chemical potential difference between the vapor and the solid product can be expressed in terms of a constant (R), temperature (T) and a measure of supersaturation, such as the ratio of partial pressures $\frac{p}{p_0}$, where p is the reactant vapor pressure and p_0 is the equilibrium vapor pressure (Equation 2.4). The above discussion is only a simple picture of a thermodynamic system. Additional thermodynamic parameters must be

considered in binary and ternary systems where there is more than one reactant involved.

$$\Delta\mu = \mu_R - \mu_P = RT \ln \frac{p}{p_0} \qquad (2.4)$$

The reactants in the vapor phase have high chemical potential. In MOVPE, this chemical potential first decreases at the boundary layer ($\Delta\mu_D$), and decreases again at the growth interface ($\Delta\mu_S$) to form the products (Figure 2.4). The boundary layer is a layer adjacent to the growth interface (between the substrate and the free gas stream) where the vapor transport occurs only by diffusion (laminar flow) [42].

One of two growth regimes may be established, depending on the fall in chemical potential. If the fall in chemical potential at the boundary layer is larger than at the interface ($\Delta\mu_D > \Delta\mu_S$), the growth is limited by the rate of mass transport (diffusion-limited), since the rate of diffusion is the limiting factor (the dashed line in Figure 2.4). Mass transport-limited growth occurs at high temperatures (above 550 °C for GaAs), where the pyrolysis of most of the precursors is almost complete. In this regime, therefore, the growth rate is not affected by changes in temperature. This regime mainly applies to the growth of ordinary layers [43].

In contrast, if the fall in chemical potential at the interface is larger than at the boundary layer ($\Delta\mu_D < \Delta\mu_S$), the growth is limited by kinetics (the solid line in Figure 2.4). Nanowire growth takes place mainly in this regime, where layer growth is suppressed and a change in temperature affects the chemical reaction rate.
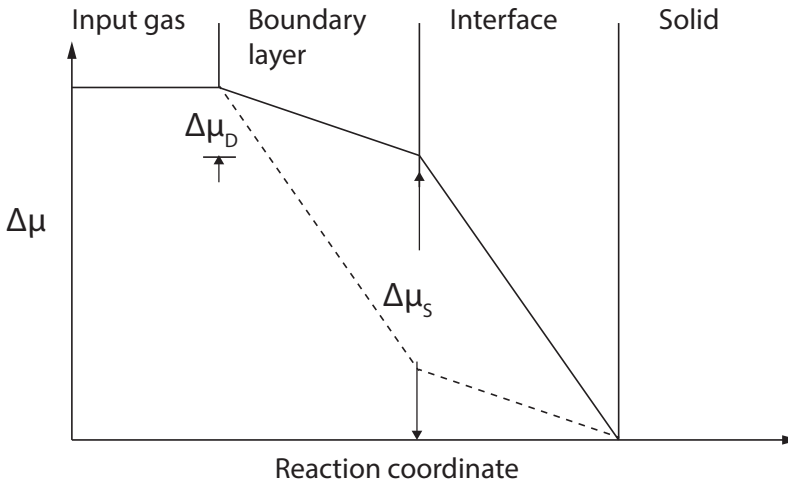

Figure 2.4 Chemical potential as a function of reaction coordinate, where the solid line illustrates the kinetics-limited growth regime and the dashed line the diffusion-limited regime.

Crystal growth

2.4. Kinetics

Kinetics describes the various reaction paths of an epitaxial growth process and determines the rates at which the reactions take place. This section reviews the reactions and defines the reaction rates for temperature-dependent processes.

The vapor-phase growth process involves gas-phase reactions (homogeneous reactions) in certain epitaxial techniques. Surface reactions (heterogeneous reactions) play important roles after materials have landed on the surface. Figure 2.5 illustrates the epitaxial growth process. Some reactants diffuse towards the substrate, after which several heterogeneous reactions and surface processes may take place. Some reactants desorb and return to the vapor phase. Some reactants diffuse on the substrate until they meet other reactants and form a nucleus, while others diffuse toward preferential nucleation sites (steps and kinks).

Several parameters determine which of the above processes occur during the growth, such as (i) surface morphology (i.e. the roughness of the surface), (ii) surface energy (Section 2.1), (iii) interactions between the reactants and the substrate (where the interface energy depends on such factors as the material and atomic plane structure), (iv) temperature (which directly affects the diffusion properties), and (v) supersaturation, which may affect the nucleation rate (Section 5.1.1).

The rate of reaction in the kinetics-limited regime depends on the temperature, and thus the reaction rate (r) can be expressed by an Arrhenius function (Equation 2.5).

$$r = A \, e^{-E_a/k_B T} \tag{2.5}$$

where the pre-exponential factor A and k_B are constants, and E_a is the activation energy.
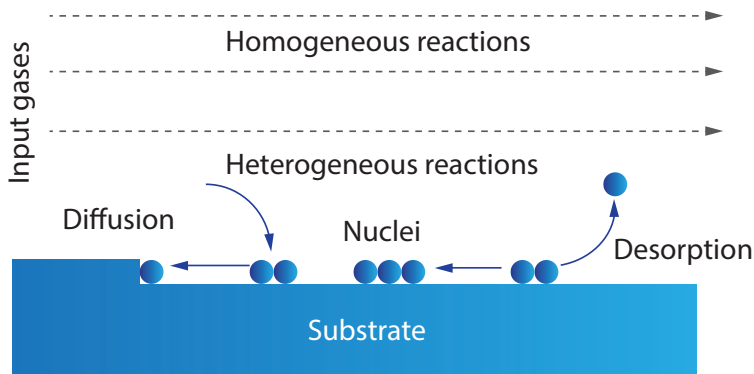

Figure 2.5 Various reactions that occur during epitaxial growth, including surface processes, homogeneous reactions and heterogeneous reactions.

It should be noted that the overall reaction rate is limited by the slowest reaction, known as the "rate-limiting step" in cases where several steps are involved. This is the case in the epitaxial growth of nanowires by MOVPE, where the nanowire growth requires the decomposition of several (at least two) precursors, and the subsequent surface diffusion of decomposition products formed.

3. Characterization techniques

Several techniques are available to determine the morphological and structural properties of epitaxially grown materials. The layers studied during the work presented here were characterized by atomic force microscopy (AFM), X-ray diffraction (XRD) and scanning electron microscopy (SEM). The nanowires were characterized by SEM and transmission electron microscopy (TEM).

3.1.   Atomic force microscopy

AFM is a scanning probe microscopy (SPM) technique in which an oscillating cantilever with a sharp tip at its end scans across a surface. The cantilever oscillates at (or near) its resonance frequency with an amplitude that is typically in a range of 20 nm to 100 nm. AFM works by maintaining a constant force between the tip and the sample, where the force (F) is calculated from Hooke's law (Equation 3.1).

$$F = -kX \tag{3.1}$$

where k is the spring constant (stiffness) and X is the cantilever deflection (distance). The constant force is typically in the range of nN to μN, in an ambient atmosphere.

AFM has three principal modes: contact, non-contact, and tapping mode (TM). TM AFM inflicts less damage on soft samples than contact AFM, and provides higher resolution data than non-contact AFM. AFM is a powerful tool that can resolve atomic-step roughness on the surface. It is, however, difficult to resolve smaller features such as kinks and adatoms on the surface.

The basic principle of TM AFM is quite simple. An oscillating cantilever with a sharp tip at its end (typically made of silicon) taps across the sample surface. The cantilever is connected to a piezoelectric scanner, and a laser beam is reflected from the cantilever's back and is monitored by a photodiode detector. A constant oscillation amplitude is maintained throughout a scan via a feedback loop that is controlled by an electronics unit. In this way, a three-dimensional (3D) picture of the surface morphology is created by analyzing the data collected from many scan lines.
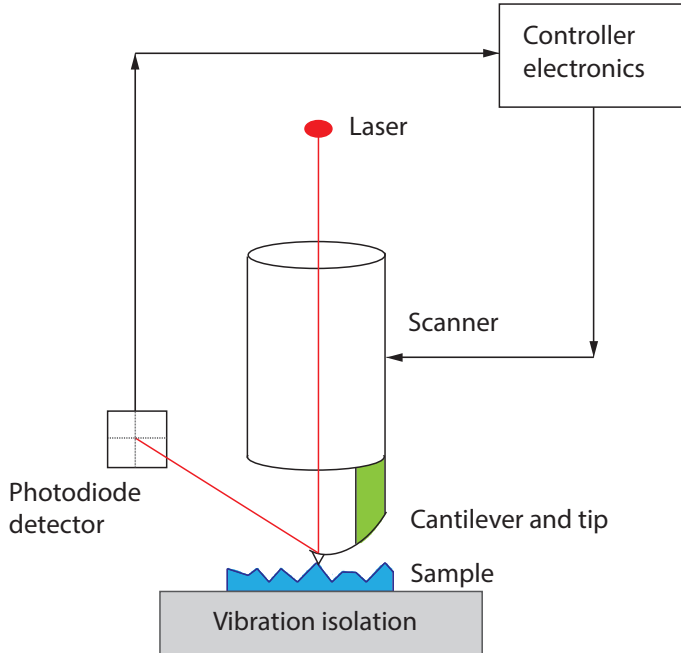
Figure 3.1 The AFM technique, in which a cantilever with a sharp tip connected to its end scans across the surface. The cantilever deflection is measured through the beam reflection by the photodiode detector. A controller unit monitors a feedback loop and maintains a constant oscillation amplitude.

A D3100 Nanoscope IIIa AFM (TM mode) was used in the study presented here to characterize the surface morphology of the InAs and GaSb layers grown, with a precision in the z-direction better than 0.1 nm. It was also used to determine the root mean square (RMS) value of the surface roughness.

3.2. X-ray diffraction

X-ray diffraction (XRD) is used to investigate the quality, composition and strain of the grown layers. High-resolution XRD was performed with a Bruker-AXS D8 system with a Cu κ-α X-ray source.

X-rays are electromagnetic waves with a wavelength in the Ångström (Å) range, which is smaller than typical atomic separations. The atoms in a crystalline material are well-ordered and they can be considered as two-dimensional (2D) planes stacked as the pages of a book (Figure 3.2a). An X-ray beam is directed at the surface at a certain angle (θ). The X-ray beam can be considered to be a plane wave that interacts with the electron clouds around the nuclei in the crystalline material.
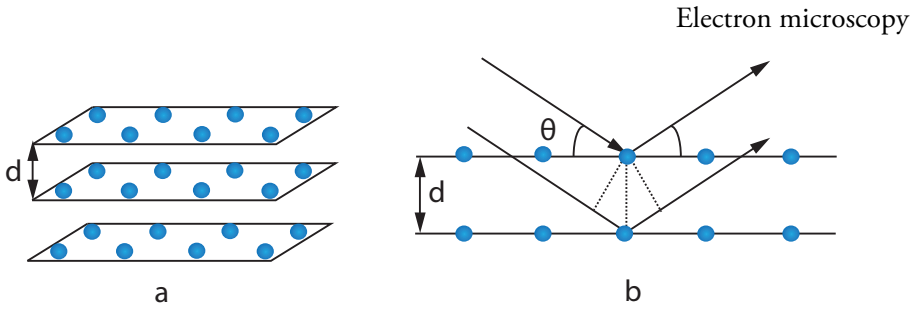
Figure 3.2 (a) 2D planes of atoms in a crystalline material positioned on top of each other with a spacing d. (b) The Bragg condition, where d is the plane spacing and θ is the angle of incidence of the beam.

The interaction causes the electron clouds to oscillate with the same frequency as that of the incident beam. This is known as "elastic scattering", which reflects the fact that the energy of the reflected beam is the same as the energy of the incident beam. Diffraction occurs when the reflected beams from the individual planes interfere constructively. This criterion is satisfied when the path difference ($2d \sin \theta$) between the beams is equal to an integer multiple of the wavelength (λ), a condition known as the "Bragg condition" (Equation 3.2). Otherwise, the beams reflected from different atomic planes interfere destructively and cancel each other out. Figure 3.2b shows the Bragg condition, where d is the atomic plane distance and is θ the angle of incidence of the beam.

$$2d \sin \theta = n\lambda \tag{3.2}$$

The diffraction pattern from a crystalline material provides various types of information about the material. Measuring the angle of incidence at the Bragg condition, for example, allows the plane spacing (d) to be calculated, and thus both the composition of the specimen and the strain within it to be determined.

3.3. Electron microscopy

Electron microscopy uses a beam of electrons to illuminate the sample and to create a highly magnified image of it. The Rayleigh criterion states that the resolution that can be obtained is approximately half of the wavelength of the incident radiation. The resolution of a light microscope is thus limited to (half of) the wavelength of visible light (μm). The resolution of an electron microscope is considerably higher than that of optical microscopes since the wavelength (λ) of an electron beam, calculated from the de Broglie equation (Equation 3.3), is much smaller. Furthermore, higher resolution can be achieved by increasing the energy of the electron beam (E), and thus creating electrons of smaller wavelengths.

$$\lambda \sim \frac{1.22}{\sqrt{E}} \qquad (3.3)$$

The interaction of the high-energy electron beam with the specimen leads to various types of scattering (Figure 3.3). Each signal obtained can be used to gain valuable information about the specimen. Some signals are detected above the specimen surface, and these are the signals used in SEM (Section 3.3.1). High-energy electron beams can pass through thin specimens, and this is the technique used in TEM (Section 3.3.2).

3.3.1. Scanning electron microscopy

SEM is one of the most common techniques used to characterize the morphology of microscale and nanoscale objects. SEM produces an image of the sample by scanning a high-energy focused beam of electrons across the sample in a raster fashion. The electron beam is created either by a thermionic source from a filament of a material such as tungsten (W) or lanthanum hexaboride (LaB_6), or by a field emission gun (FEG).The beam is focused by passing it through several condenser lenses. Scan coils are used to control the scan procedure.

One type of signal produced by inelastically scattered electrons is called secondary electrons (SEs). These are valence electrons of the sample that have been knocked out of the specimen by the beam electrons.

Most SEs are re-absorbed by the sample, and only those that are produced from approximately the top 5 nm of the sample are detected. These electrons have energies of less than 50 eV. SEs generated from deeper parts of the sample are re-absorbed before they reach the surface, and the interaction volume between the beam and the sample is small. Thus SEs give images with a high spatial resolution. SEs give a topographic image, since the electrons come from (near) the surface.

Elastic interactions between the electron beam and the nuclei of the atoms in the sample generate backscattered electrons (BSEs). BSEs are generated homogeneously down to a certain depth, the magnitude of which is determined by their high energy (defined by the electron beam). Such electrons, thus, may originate from deeper parts of the sample, and may spread out more, giving images with poorer spatial resolution than those produced from SEs. The fraction of beam electrons that undergo backscattering depends on the atomic number of the elements in the sample (Z). For this reason, backscattered electrons are commonly used to investigate materials with components of very different atomic numbers, where the higher Z elements appear brighter.
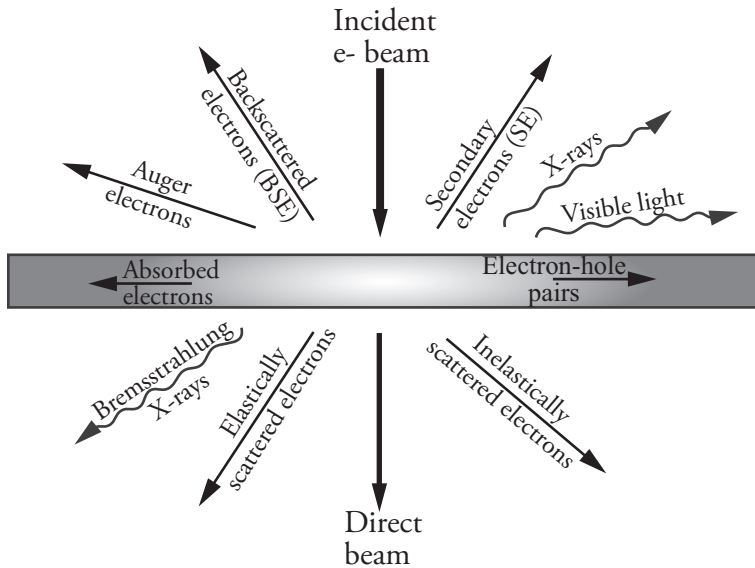
Figure 3.3 Interaction of the high-energy electron beam with the specimen generates various types of electrons (straight arrows) and photons (wavy arrows) [Courtesy of K. Hillerich].

In the work presented in this thesis, SEs were detected and analyzed to obtain the surface topography of various types of sample. The surface morphology of the layers and nanowires was evaluated by an FEI Nova NanoLab 600 and a LEO 1560.

3.3.2. Transmission electron microscopy

TEM is one of the most sophisticated characterization tools available, and it provides valuable detailed information about the specimen, including information about the atomic arrangement, the presence and type of crystal defects, and the chemical composition. TEM requires a high-energy beam and a thin sample (less than approximately 100 nm for most semiconductors), so that the beam can pass through the sample. Elastically scattered electrons produce electron diffraction patterns from crystalline samples, which give information about the atomic plane separation at that particular angle. Diffraction patterns are commonly used to determine the crystal structure of samples.

TEM can be used in various operating modes, which differ in beam alignment (convergent or parallel) and the magnitude of the condenser lens aperture. The work presented here has used high-resolution TEM (HRTEM), X-ray energy dispersive spectroscopy (XEDS) and high-angle annular dark field scanning TEM (HAADF STEM) to determine the structural and compositional properties of the nanowires.

Characterization techniques

In TEM mode, a parallel beam is used to illuminate the sample, and the transmitted direct beam and elastically scattered electrons are used to form an image. The incident beam is parallel also in HRTEM, which reveals the atomic structure of crystalline specimens. The beam is focused to a point and scanned across the specimen in STEM (just as in SEM), and the direct beam, diffracted beam and beam scattered at high angles are collected and analyzed. The electrons scattered at high angles can be used to create high-angle annular dark field (HAADF) images in which the contrast is depends mainly on the chemical composition of the sample and its thickness.

Inelastic interactions of the primary beam with the specimen generate a variety of secondary signals including SEs, Auger electrons and X-rays. When the high-energy electron beam interacts with the specimen, electrons may be ejected from the inner shells of atoms, leaving electron vacancies. The electrons from the outer shells then fill those vacancies. The energy difference between the outer shell and the inner shell can be released as X-rays whose wavelengths are characteristic of the elements in the sample. The energy may also eject an electron from the same atom, giving what are known as "Auger electrons". Therefore, detecting the X-rays is a powerful technique used to determine the chemical composition of the specimen. This technique, known as X-ray energy dispersive spectroscopy (XEDS), is commonly used with the HAADF STEM mode to obtain a spatially resolved map of the chemical composition of the sample.

We have used a JEOL 3000F TEM to obtain various types of information about the nanowires, such as their crystal structure and composition. Nanowires were broken off from the substrate and mechanically transferred onto carbon-coated copper grids before TEM characterization.

4. Layer growth

This chapter introduces the fundamental principles of III-V layer growth and discusses the growth results achieved during the work presented in this thesis. Section 4.1 introduces the fundamental principles of layer growth, while Section 4.2 presents the layer growth results. Sections 4.2.1 and 4.2.2 describe an investigation into the epitaxial growth of GaSb and InAs layers on Si (111) substrates. Section 4.2.3 describes an investigation into the epitaxial growth of GaSb layers on InAs-Si (111) substrates.

4.1. Fundamental principles of layer growth

The integration of high-mobility III-V semiconductors such as InAs and GaSb with Si substrates has significant potential for several device applications, such as long-wavelength infrared detectors [48, 49]. However, epitaxial growth of InAs and GaSb on Si substrates presents several challenges, such as lattice mismatch, thermal mismatch and the formation of anti-phase domains (APDs).

Epitaxial growth of lattice-matched materials can lead to the formation of perfect crystals. However, epitaxial growth of lattice-mismatched materials forces atoms of the epitaxial layer to follow the periodic order of the substrate material, which results in the creation of strain (ε) in the epitaxial layer. The strain that is created is linearly related to the lattice mismatch value (Equation 4.1).

$$\varepsilon = \frac{a_0 - a}{a_0} \qquad (4.1)$$

where a_0 is the epitaxial layer lattice constant and a is substrate lattice constant. Several layers can be grown grow epitaxially until the strain energy becomes too large. At this stage, the epitaxial layer will relax and release this energy. The strain energy can be released either by dislocation formation (which occurs preferentially in systems with low lattice mismatch, Figure 4.1a), or by what is known as "Stranski-Krastanov (SK) island formation" (Figure 4.1b). One type of dislocation that occurs often during the epitaxial growth is the "misfit" dislocation. The epitaxial layer minimizes the strain through the omission of some atomic planes, as shown by dashed lines in Figure 4.1a.

Layer growth

The magnitude and the direction of the lattice distortion can be described by a vector, known as the "Burgers" vector. In the case of a misfit dislocation, the Burgers vector is parallel to the growth plane (the growth interface), shown by the red arrow in Figure 4.1a. This type of dislocation is often preferred since it does not propagate along the growth direction. The Burgers vector may have other orientations relative to the substrate in other types of dislocation, and such dislocations can propagate upward through the grown layer. These types of dislocations are not favorable, since they degrade the film quality and adversely affect electrical and optical properties of the epitaxial layer (epilayer). We have studied also screw dislocations (Figure 4.1c). Screw dislocations arise when the shear stress forces half of a plane to slip across the other half, and in this way distort the atomic arrangement. The Burgers vector of a screw dislocation is perpendicular to the growth interface (shown by the red arrow in Figure 4.1c).

Thermal mismatch between the substrate and epilayer is another cause of dislocations. Thermal mismatch is the term used to describe a situation in which the substrate and epilayer have different thermal expansion coefficients. Thermal cracks may also arise if the difference in thermal expansion coefficient is very large [50].

The growth of a polar material on a non-polar substrate introduces further aspects. During the growth of an InAs layer on a Si substrate, two precursors (indium and arsenic) bind to the Si atoms of the substrate. The presence of atomic steps on the Si substrate may, therefore, create two different types of domain, Group III-terminated and Group V-terminated domains, known as APDs [50, 51]. The formation of APDs is also related to the crystal orientation of the substrate. A Si (211) substrate, for example, is advantageous over Si (111) and Si (100) substrates, since it provides two clear sites for atoms to bind, which lowers the APD density [52]. Also, single domain GaAs layers can be grown on misoriented Si (100) substrates, due to double-step formation and self-annihilation mechanism [51].
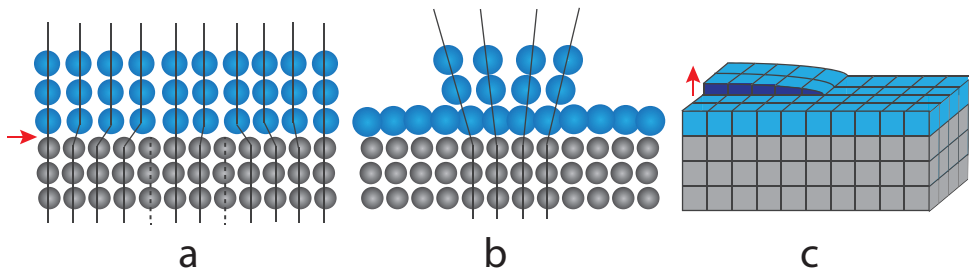

Figure 4.1 (a) Misfit dislocation formation when the lattice mismatch is rather low. The Burgers vector (red arrow) is parallel to the growth plane. (b) SK island formation for high lattice mismatch. (c) A screw dislocation in which the shear stress distorts the atomic arrangement. The Burgers vector (red arrow) is perpendicular to the growth plane.

Surface preparation is key to the successful epitaxial growth of III-V materials on Si substrates. A clean Si substrate has a high surface energy and tends to absorb impurities to lower this. Contaminants on the substrate surface adversely affect the nucleation process and may contaminate the epitaxial layers. A contaminant may act as a preferential nucleation site and perturb the non-preferential nucleation sites for Group III and V elements. Depending on the type of contamination and surface morphology, contaminants may act like steps on the surface and result in APD formation. It is, therefore, vital to clean the substrate surface properly. The surface of a Si substrate, in addition, becomes covered by a layer of native oxide when exposed to air.

Extensive studies on Si surface cleaning took place during the 20th century, due to the importance of Si for the semiconductor technology. Several chemical cleaning methods, such as Shiraki [53] and RCA cleaning [54], were developed to effectively remove any contamination from the Si surface. We have used the RCA process, which removes surface contaminants and protects the surface by oxide formation, to clean the Si wafers. The oxide layer was subsequently etched by HF treatment to form an H-terminated surface, and the samples were then directly transformed to the growth reactor.

In the case of the growth on III-V substrates, prior to the growth, the native oxide or so-called "epi-ready" oxide (provided by the vendor) should also be removed. Different chemical processes and annealing processes are suitable for different materials. Annealing of III-V substrates at high temperatures, however, may cause decomposition at the surface of the material. The decomposition temperature is related to the binding energy of the corresponding material [55], which is lowest for InSb and GaSb materials. This means that the Group V material (which is more volatile than he Group III material) should be supplied during the annealing procedure, to avoid surface decomposition. The native oxide may instead be removed by chemical cleaning, and the sample should be immediately transferred to the growth reactor. Clawson [56] provides a list of wet chemical etchants for III-V semiconductor materials.

InSb and GaSb are the III-V materials that are most sensitive to oxidation [57]. GaSb, in particular, forms a thick oxide layer, including Ga_2O_3, which requires a very high annealing temperature to remove [58]. The presence of hydrogen during the annealing step reduces the de-oxidation temperature [58, 59]. Hydrogen is often used as the carrier gas in MOVPE, and this allows a lower annealing temperature to be used, which helps to avoid severe decomposition at high temperatures.

Nucleation is the second key step that needs to be considered. In the work presented here, a Group V-terminated surface was created by exposing the H-terminated surface (formed by HF treatment) to the Group V flow. A nucleation step was necessary in cases of high lattice mismatch. This was the case, for example, for InAs and GaSb layer growth on Si substrates (~12% lattice mismatch), and a two-step growth

approach was used. This method has been applied in several material systems with large lattice mismatches, such as GaAs layer growth on Si substrate [50, 60]. In the two-step growth approach, growth starts at a low temperature (to form a nucleation layer) and subsequently continues at a higher temperature (to form the second layer).

4.2.   Layer growth results

We have used a two-step growth approach to grow GaSb and InAs layers on Si (111) substrates. The nucleation layer was grown at a relatively low temperature and relatively high V/III ratio, to limit surface diffusion of the reactants and to form a high density of SK islands. The surface was subsequently annealed briefly at a higher temperature to enhance a process known as "Ostwald ripening" and to improve the surface coverage. Ostwald ripening is a consequence of the size dependence of the vapor pressure, where smaller islands have higher vapor pressure than larger ones. This gives rise to a concentration gradient in the vapor phase, and material is transferred from smaller to larger islands. Larger islands grow and smaller islands shrink and finally disappear [61]. The second layer was subsequently grown at high temperature and low V/III ratio, to favor adatom mobility.

4.2.1.   GaSb layer growth on Si (111)

GaSb is a promising material with several interesting properties. It has, for example, a direct narrow band gap, which is required for electro-optical application in the near infrared range [62]. Undoped bulk-grown GaSb is p-type, and can be either n-type or p-type doped. Sulfur (S), selenium (Se) or tellurium (Te) can be used for n-type doping, while germanium (Ge), tin (Sn) or beryllium (Be) can be used for p-type doping [62].

Manasevit and Hess demonstrated in 1979 that GaSb layers can be grown by metalorganic chemical vapor deposition (MOCVD) [63]. This led to several studies on the growth of GaSb layers [64-66]. These studies focused mainly on the epitaxial growth of GaSb layers on III-V or sapphire substrates. III-V substrates are much more expensive than Si substrates. Furthermore, Si substrates offer several key advantages over III-V substrates: they are robust, available in large sizes, have high thermal conductivities, and expertise in Si-based technology is widely available. Additionally, the epitaxially grown GaSb layers on Si (111) substrates can serve as substrates for the growth of vertical GaSb nanowires. This section describes the epitaxial growth of GaSb layers on Si (111) substrates.
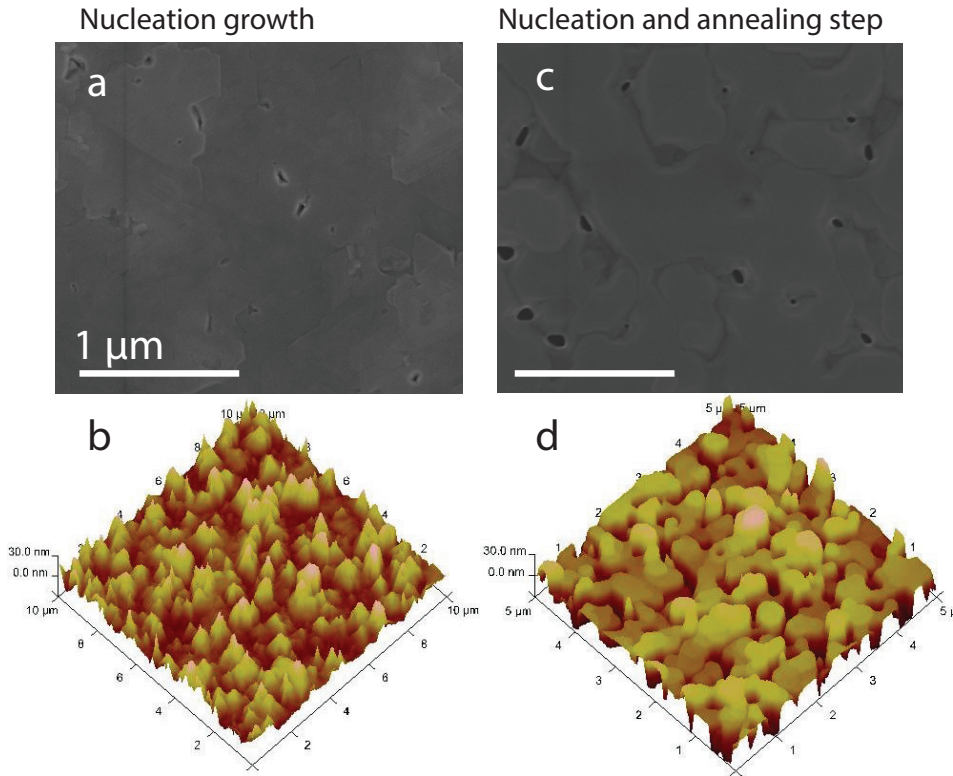
Nucleation growth   Nucleation and annealing step

Figure 4.2 (a) Top-surface SEM image of the GaSb nucleation layer. (b) 10×10 μm^2 AFM image of the GaSb nucleation layer. (c) Top-surface SEM image of the same sample after annealing at 600 °C for 5 min, showing larger holes on the surface. (d) 5×5 μm^2 AFM image of the annealed sample, showing lower surface roughness.

We have studied the growth of GaSb epitaxial layers on Si substrates through a two-step approach, since there is a large lattice mismatch between GaSb and Si (~12%).

Triethylgallium (TEGa) and trimethylantimony (TMSb) were used as precursors. TEGa is better than the more commonly used TMGa, since TEGa pyrolysis occurs at a temperature approximately 100 °C lower than that at which TMGa pyrolysis occurs. This means that the growth of GaSb layers when using TEGa as source is mass transport-limited in the temperature range of 525-640 °C. The growth is kinetically limited when TMGa is used as source [67]. Therefore any fluctuation in the growth temperature has only a minor effect on the growth rate, when TEGa is used as source.

Several processes that occur during the GaSb layer growth were investigated, including formation of an Sb-terminated surface, nucleation, annealing, and growth of the second layer. The H-terminated surface was first replaced by an Sb-terminated

surface to initiate the growth. We studied a series of samples with the same nucleation growth parameters, varying the initial annealing temperature between 500 and 600 °C, and varying the Sb flow time from 10 sec to 1 min. We then characterized the surface morphology of the samples produced by AFM and SEM.

A flow of Sb for 10 sec at 600 °C gave the greatest degree of surface coverage and the lowest RMS value of roughness (~8.25 nm). Figures 4.2a and 4.2b show SEM and AFM micrographs of this sample. The improvement in morphology that arises by reducing the Sb flow time is probably related to the low equilibrium vapor pressure of antimony, which causes excess material landing on the surface to remain there [68, 69]. Sb termination is a key step in obtaining high quality GaSb layers [70]. However, the low equilibrium vapor pressure of antimony makes it difficult to obtain such a layer. This has led several groups to consider using a thin buffer layer of AlSb to initiate the growth [71-75]. Proessdorf *et al.* [76] investigated the MBE growth of GaSb layers on Si (111) substrates. They used RHEED to demonstrate that the initial Si surface reconstruction affects the surface morphology [76].

We have grown nucleation layers from TEGa with a molar fraction of 1.1×10^{-4} and from TMSb with one of 4.01×10^{-4} (V/III ~3.6). Further AFM studies on the nucleation growth temperature and time showed that 10 min growth at 450 °C provides the greatest degree of surface coverage and smoothest sample. Figures 4.2a and 4.2b show the SEM and AFM images of the sample obtained with these nucleation growth parameters. The large lattice mismatch between GaSb and Si substrates means that we expect stacking faults to be present at the interface.

We investigated the effect of the annealing on the samples by changing the annealing temperature from 550 to 600 °C and the time from 2 to 5 min. AFM images of samples created under different annealing conditions showed that surface morphology is optimal (at those areas without holes) after annealing at 600 °C for 5 min (Figure 4.2d). The SEM image (Figure 4.2c), however, showed that the size of the holes on the surface increased, probably due to an increase in diffusion length of reactants on the surface.

We next studied the formation properties of the second layer. Lowering the V/III ratio (at 600 °C) considerably improved the surface roughness. It should be mentioned that only the molar fraction of TMSb was decreased, from 2.17×10^{-4} (V/III ~2) to 1.08×10^{-4} (V/III ~1), and that the second layer growth was performed at 600 °C for 10 min.

Figures 4.3a and 4.3b show AFM and SEM images of the sample produced at the higher molar fraction of TMSb (2.17×10^{-4}). The RMS value of the roughness of these samples was ~40 nm. However, the sample produced with the lower TMSb molar fraction (1.08×10^{-4}) looked almost mirror-like (Figure 4.3d). The RMS value of roughness for the specimen created at a lower TMSb flow was ~15 nm in the areas without holes.
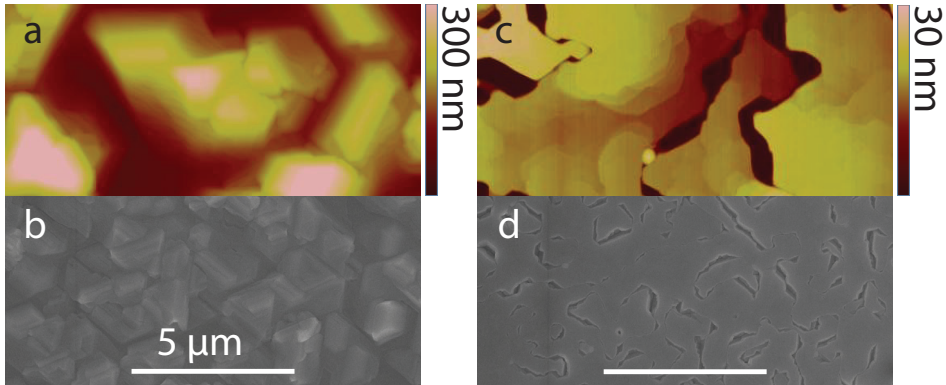
Figure 4.3 (a) 2.5 × 5 μm² AFM image of GaSb surface after the second layer growth (V/III ~2), showing a very rough surface. (b) Top-surface SEM image of the same sample. (c) 2.5 × 5 μm² AFM image of GaSb layer with lower TMSb flow (V/III ~1), showing quite a smooth surface. (d) Top-surface SEM image of lower TMSb flow sample showing that some holes remained on the surface.

The observed significant effect of the V/III ratio on the surface morphology agrees with previous reports [65, 68, 69, 77], which showed that a V/III ratio of around unity is crucial to suppress Ga-rich or Sb-rich regimes. Furthermore, increasing the GaSb layer thickness decreases the surface roughness and the defect density, due to the formation of the close dislocation loops [78, 79].

4.2.2. InAs layer growth on Si (111)

The high electron mobility and narrow band gap of InAs make this a promising material with applications in various devices [52]. InAs layers grown on GaAs substrates (where the lattice mismatch is 7.2%) are interesting in infrared detectors and lasers [80-86]. The epitaxial growth of InAs layers on Si substrates is more challenging than the epitaxial growth of InAs on GaAs substartes, due to the larger lattice mismatch of 11.6%. Hsu *et al.* [87] have shown that high quality InAs materials can be grown as nanofins, by patterning the Si substrates. The epitaxial growth of InAs layers on Si substrates has been studied by several groups [52, 88-93]. This section describes the epitaxial growth of InAs layers on Si (111) substrates. The use of the Si (111) substrates facilitates the nanowire growth.

InAs layers were grown on Si substrates using a two-step approach, since the lattice mismatch was so large (11.6%). We used trimethylindium (TMIn) and arsine (AsH$_3$) as precursors. It should be mentioned that tertiary-butyl arsine (TBAs) or phenylarsine (PhAs) can be used instead of the AsH$_3$ source.
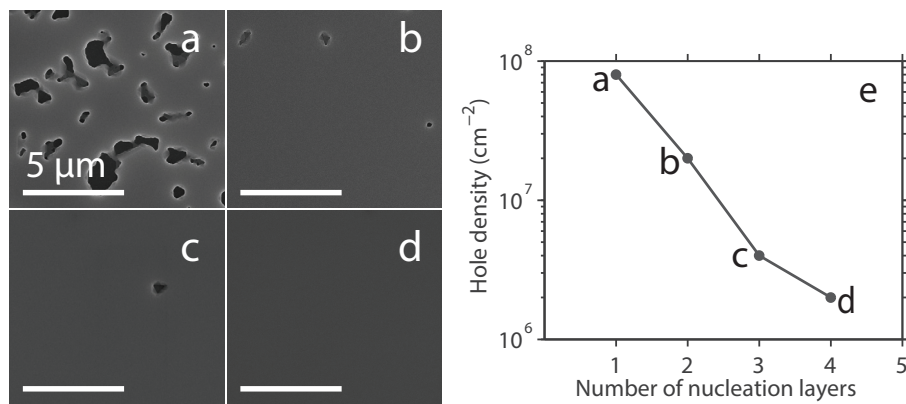
Figure 4.4 Top-surface SEM images of InAs epitaxial layer with (a) one, (b) two, (c) three, and (d) four nucleation layers. (e) The hole density on the surface decreases significantly as more nucleation layers are added. The figure has been adapted from Paper I.

Haywood *et al.* [82] have shown that using TBAs and PhAs sources improves the electrical properties and surface quality of the layers, since these precursors have lower pyrolysis temperatures than that of AsH_3. Paper I describes the experimental details used to grow the InAs layers. InAs layers grown on Si (111) with one nucleation layer have a high density of holes on the surface [94, 95]. Adding more nucleation layers decreases significantly the density of holes on the surface (Figure 4.4e). Figures 4.4a-d show top-surface SEM images of samples with one to four nucleation layers. An epitaxial layer of approximate thickness 200 nm (the second layer) was grown on top of the nucleation layers.

AFM of the samples revealed that the surface root mean square roughness (RMS) of a sample with one nucleation layer was 1.5 nm in a flat region (an area without holes). This value was 0.7 nm for the sample with two nucleation layers and 0.4 nm samples with more than three nucleation layers. Figure 4.5a shows an AFM image of an InAs epitaxial layer with five nucleation layers, where Figure 4.5b shows the derivative of this image. InAs grows as triangular nuclei in a step-flow manner, where the step heights correspond to the InAs lattice constant.

XRD characterization of the samples with one to six nucleation layers showed that the quality of the film was improved by incorporating additional nucleation layers. The improvement was expressed as the clear presence of Pendellösung fringes on both sides of the InAs peak. Figure 4.5c shows 2θ/ω spectra of samples with one to four nucleation layers, where the inset shows FWHM values. The decrease in the FWHM value from 70 to 53 arcsec shows that the quality improves as the number of nucleation layers increases. Paper I gives further details.
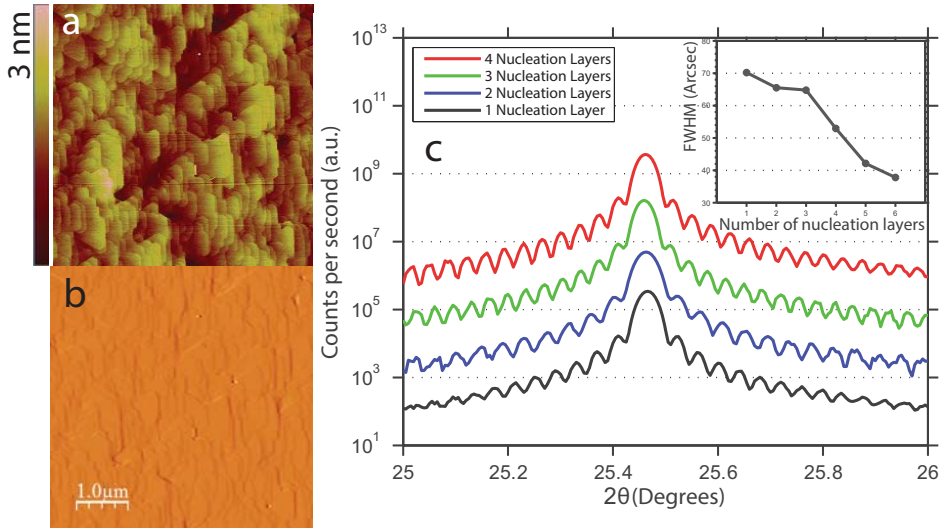
Figure 4.5 5 × 5 µm² of (a) AFM image (b) derivative AFM image of InAs epitaxial layer grown using five nucleation layers. (c) High-resolution 2θ/ω scans of samples with one to four nucleation layers, where subsequent signals have been shifted upwards for clarity. The inset shows FWHM values taken from the rocking curve for one to six nucleation layers. The figure has been adapted from Paper I.

The structural characterization described above confirmed that InAs epitaxial layers formed by adding four nucleation layers were of high quality. Adding more than four nucleation layers did not further improve the film quality.

After the successful growth of small samples, InAs epitaxial layers (with four nucleation layers) were grown on a full 2" Si wafer. This epitaxial layer could be used as the substrate for nanowire growth. Paper II describes studies of the growth of InAs nanowires growth on the InAs epitaxial layer over 2" wafer, where the wires were homogeneous across the entire 2" wafer.

4.2.3. GaSb layer growth on InAs-Si (111)

The type II band alignment of the GaSb-InAs heterostructure provides an interesting system for various device applications, such as tunneling devices, in which the GaSb valence band has a higher energy than the InAs conduction band [8, 96]. In addition, InAs and GaSb both belong to the 6.1 Å family and are almost lattice-matched [97]. This makes it possible to grow GaSb on InAs layers in a one-step approach (in contrast to the two-step growth approach that must be used for highly mismatched materials).
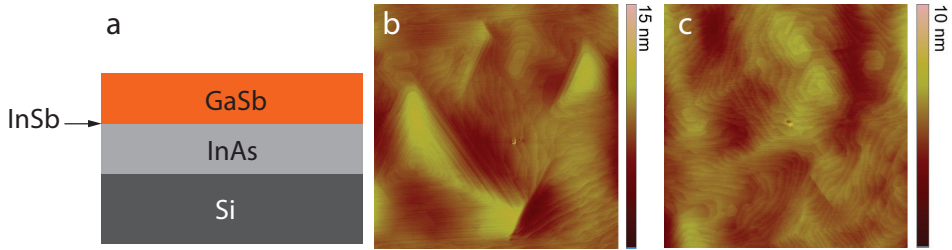
Layer growth

Figure 4.6 (a) The structure of a sample with a GaSb layer grown on an InAs epitaxial layer grown on a Si (111) substrate. (b) 5 × 5 μm² AFM image of GaSb surface grown with V/III ~2, and (c) 5 × 5 μm² AFM image of GaSb surface grown with V/III ~1, showing the improved morphology. The figure has been adapted from Paper I.

Several groups have studied epitaxial growth of the InAs-GaSb heterostructure, mainly on GaAs and GaSb substrates [8, 48, 79, 96, 98, 99]. GaAs-type or InSb-type interfaces can be constructed by using different switching sequences [96, 98]. The direct growth of GaSb layers on a Si (111) substrate is difficult (Section 4.2.1). The indirect growth of the GaSb layers (on the InAs buffer layers) is an alternative approach that may be more successful, given the interesting properties of GaSb-InAs. This section describes studies into the epitaxial growth of GaSb layers on InAs layers grown on Si (111) substrates (Section 4.2.2).

We constructed an InSb-type interface (Figure 4.6a) with simultaneous switching between In and Sb, with a 3 sec pause for Ga and As. The V/III ratio has a significant effect on the surface morphology of the GaSb layers grown (Section 4.2.1). This is the case also for GaSb layers on an InAs layer, using various molar fractions of TMSb [8]. Paper I presents the detailed growth parameters of these samples.

Figures 4.6b and 4.6c are AFM images of the GaSb surface morphology grown with V/III ratios of 2 and 1, respectively. The AFM images show several clockwise and anti-clockwise spiral mounds on the GaSb surface [100, 101]. We correlate these to screw dislocations that originate from steps on the InAs surface. A lower molar fraction of TMSb gives spiral mounds on the surface with lower sizes and heights, and thus the surface morphology is better. The rather low density of the spiral mounds also reflects the high quality of these InAs epitaxial layers [101].

5. Nanowire growth

"Nanowires", as the name implies, are structures with a nanoscale size in two dimensions and a microscale size in the third dimension. Nanowires can be fabricated by two different approaches: "top-down" and "bottom-up". Nanowires are carved out of a bulk crystal material in the top-down approach, while they are fabricated through synthesis, reaction, and self-assembly in the bottom-up approach. These processes are most often initiated from a substrate.

The work presented here focuses exclusively on a bottom-up approach in which nanowires have been epitaxially grown from precursors. The fundamental principles of III-V nanowire growth are introduced in Section 5.1. The growth of antimonide-based nanowires is discussed in Section 5.2, focusing on the differences between antimonide-based nanowires and arsenide-based and phosphide-based nanowires. Section 5.2 discusses difficulties in growing such nanowires. Finally, Section 5.3 discusses complex nanowire structures, including axial and radial heterostructures, and ternary nanowires.

5.1. Fundamental principles of nanowire growth

Nanowires are often grown using metal catalyst seed nanoparticles, which increase the rate of reaction close to the nanoparticles. The growth direction of the nanowires is determined by the total free energy of the system and by the free energy of the particle/substrate interface.

For diamond and zinc-blende crystal structure compounds such as Si and GaAs, the growth often occurs in <111>-type directions, since the {111} particle/substrate interface type has the lowest energy [102, 103]. The <111>-type directions can be classified either as <111>A (Group III-terminated) or <111>B (Group V-terminated) directions, where the latter is the lower energy plane [104]. The epitaxial growth of nanowires on a <111>B substrate, such as GaAs and InAs, results mainly in the growth of vertical nanowires (grown along the <111>B direction). It is possible to change the nanowire growth direction by engineering the surface and interface energies [105-108].

Nanowire growth

Gold (Au) is by far the most commonly used catalyst seed particle material [109]. Several reports have recently been published of successful nanowire growth using alternative seed particles, such as Cu for InP [110, 111], Ag for InSb [112], Pd for InAs [113-115], Ni for GaAs [116, 117], Al for Si [118], Mn for InAs [119], and Mn also for Ge and Si nanowires [120, 121]. However, Au remains the most closely studied seed material for many nanowire compositions. Figure 5.1a shows Au-seeded nanowire growth.

Au can be deposited by several methods [122]. We have used two different techniques: based on Au aerosol nanoparticles or lithographically patterned Au nanoparticles. In the first approach, Au aerosol nanoparticles with a well-defined size and diameter are randomly deposited onto the substrate surface [123]. In the second approach, the positions of the Au nanoparticles are lithographically defined on the substrate surface. The first approach is fast, clean and cheap, while the second approach offers a key advantage in "positioning". This is essential when making nanowires to be used in devices, where precise alignments are required. Paper II describes how we used the second approach to verify the high quality of the InAs buffer layers, and demonstrated successful growth of InAs nanowires with various diameters and pitches across a 2" wafer.

Nanowires can be grown also using "catalyst-free" and "self-catalyzed" approaches. The catalyst-free approach requires a template, such as an oxide mask, to restrict the growth, and the technique is known as "selective area epitaxy" (SAE). Growth in SAE is limited to certain areas of the surface (Figure 5.1b).

This mask preparation technique was used in the study reported in paper V where prior to the growth Si wafers were chemically treated (HF treatment) and transferred to the growth chamber after the chemical treatment. A thin layer of native silicon oxide (SiO_x) forms on the surface immediately after the chemical treatment, and this acts as an oxide mask. The SiO_x layer contains nanoscale apertures at which nanowire growth can start. Other than that the growth on the oxide surface (i.e. in areas without apertures) is suppressed [124].

Paper V describes experiments in which growth was initiated by a Ga flow that formed Ga nanoparticles inside the oxide apertures.
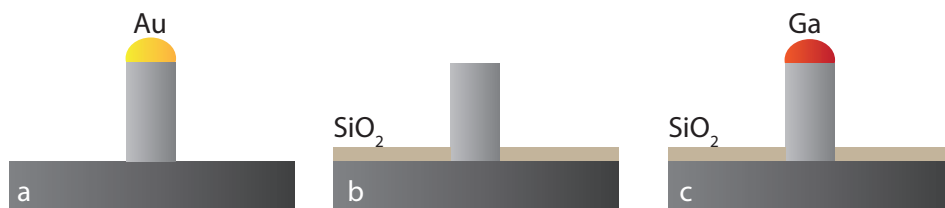

Figure 5.1 (a) Au-seeded nanowire growth, (b) Nanowire growth using the SAE approach, and (c) Ga-assisted nanowire growth.
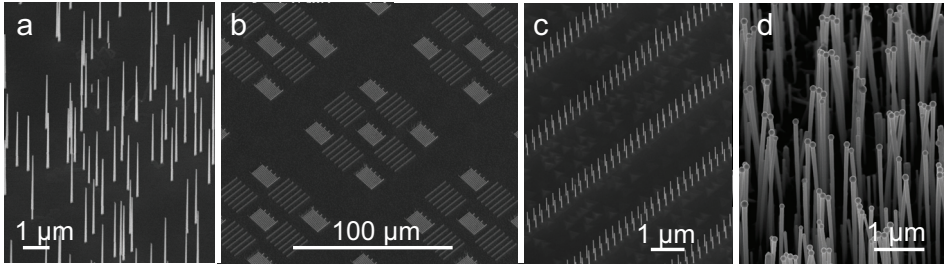
Figure 5.2 30° tilted SEM images of (a) GaAs nanowires grown from Au aerosol nanoparticles, (b) InAs nanowires grown from lithographically defined Au patterns with various diameters (25-55 nm) and pitches (200, 300, and 500 nm) on InAs buffer layers on Si substrates. (c) High-magnification SEM image of part of (b), showing the ordered nanowire arrays, and (d) Ga-assisted GaAs nanowires grown directly on Si (111) substrates. The SEM images in (b) and (c) have been adapted from Paper II.

Ga-assisted growth proceeds in a manner very similar to that of Au-assisted growth, where the Group III element (Ga) that is to form the nanowire is used as catalyst material rather than an external material such as Au (Figure 5.1c).

Figure 5.2 shows SEM images of several nanowires grown with the techniques described above. Figure 5.2a is an SEM image of GaAs nanowires grown from Au aerosol nanoparticles, and shows random positioning. Figures 5.2b and 5.2c are SEM images of InAs nanowires from lithographically defined Au patterns grown on InAs layers on a Si (111) substrate (Paper II). Figure 5.2d is an SEM image of Ga-assisted grown nanowires on a Si (111) substrate (Paper V).

5.1.1. Nucleation theory

Wagner and Ellis [125] presented the first model that described the spontaneous growth of Au-seeded Si whiskers. They proposed what they called the "vapor-liquid-solid" (VLS) growth mechanism to explain the growth of the Si whiskers, and related the formation of the liquid particles to the low eutectic melting point of Au-Si alloy. This section presents the classical nucleation theory model used to explain nanowire growth.

The unidirectional growth of catalyst-seeded nanowires can be understood by considering the change in Gibbs free energy that occurs when a solid nucleus forms at the triple-phase boundary (TPB), where the vapor, liquid and solid phases meet. The Gibbs free energy of a spherical nucleus can be calculated from Equation 5.1.

$$\Delta G = -\Delta\mu \frac{V}{V_{mn}} + \gamma_n A_n \qquad (5.1)$$

Nanowire growth

The first term on the right-hand side describes the energy reduction when a nucleus forms, where V and V_{mn} are the nucleus volume and nucleus molar volume, and where $\Delta\mu$ is the chemical potential difference of the species (the atoms that form the crystal) in the supply phase and the solid crystal phase. The second term on the right-hand side describes the energy added to the system, due to formation of the new surface/interface, where γ_n and A_n are the nucleus interface energy and area, respectively. Equation 5.1 allows the critical nucleus size (where the Gibbs free energy is maximized) to be calculated. Nuclei with sizes greater than this and less than this have lower Gibbs free energies. The increase that occurs in the nucleus size to decrease the Gibbs free energy causes nanowire growth. Nuclei that are smaller than the critical nucleus size must lower their energy by shrinking, which causes them to become unstable.

Recent *in situ* studies have greatly advanced our understanding of the nanowire growth mechanism. These studies revealed that the nanowire growth often occurs by nucleation of a single step (a monolayer of Group III atoms and a monolayer of Group V atoms) from one side, followed by the flow of the step across the nanoparticle/nanowire interface (in what is known as the "growth front") [126]. Therefore, by considering the nanowire geometry with hexagonal cross section, the spherical nucleus shape could be modified (Figure 5.3). If we now consider a spherical crystalline nucleus, with liquid vapor (γ_{lv}), liquid solid (γ_{ls}) and solid vapor (γ_{sv}) interfacial energies, Equation 5.1 becomes:

$$\Delta G = -Ah\Delta\mu + Ph\gamma_{ls}(1-x) + Ph\gamma_{sv}x - Ph\gamma_{lv}x\sin\beta \qquad (5.2)$$

where A, h, P, and β are the nucleus surface area, height (often one monolayer), perimeter and the catalyst/nanowire contact angle. The first term on the right-hand side of Equation 5.2 describes the energy reduction due to the formation of the crystalline nucleus. The other three terms on the right-hand side of Equation 5.2 describe the changes in the interfacial energies, where x is the fraction of the nucleus that is in contact with vapor. The second term describes the interfacial energy between the liquid and solid nanowire. The third term describes the interfacial energy between the x fraction of solid nucleus and vapor. The fourth term describes the interfacial energy for the x fraction of the liquid catalyst that has been replaced by the nucleus [127-129].

It is possible in the same way to calculate the Gibbs free energy change for nucleation at other possible positions, including substrate surface and nanowire side facets. The supersaturation term is the same, and thus only the interfacial energy terms differ.
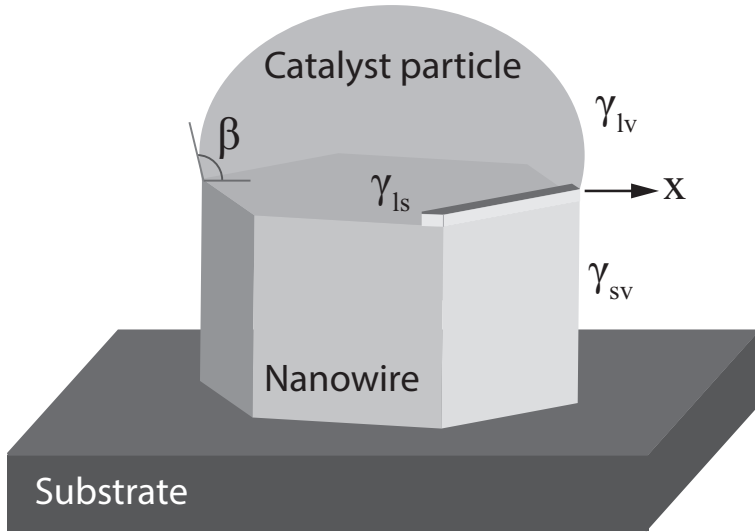
Figure 5.3 The formation of a nucleus at the catalyst/solid nanowire interface with catalyst vapor (γ_{lv}), catalyst solid (γ_{ls}) and solid vapor (γ_{sv}) interfacial energies. The fraction of the nucleus in contact with vapor is shown by x, and the catalyst/nanowire contact angle is β.

The unidirectional growth of the nanowires can thus be explained by the lower interfacial energy terms (lower interfacial energies at the liquid/solid interface than at the solid/vapor interface) at the TPB than on the substrate surface or nanowire side facets.

The model described is based on an assumption that the catalyst particle is in the liquid state during nanowire growth. This is known as the "VLS" growth mode. Several groups have reported that growth occurs with solid catalyst seed particles, in a mode known as the "vapor-solid-solid (VSS)" growth mode [113, 130, 131]. The VSS growth mode explains the epitaxial growth of nanowires below the eutectic point of the corresponding alloy nanoparticles. Recent *in situ* studies of Au-seeded Ge nanowires revealed that the Au nanoparticles are liquid even below the eutectic temperature, which was attributed partly to the nanoscale size effect [132]. Kodambaka *et al.* [132] have shown that Au-seeded Ge nanowires grow with either liquid or solid catalyst particles (VLS or VSS) at the same temperature. Cu-seeded InP nanowires also grow simultaneously in these two growth modes [111], as do Pd-seeded InAs nanowires [113]. Nanowires grown by the two modes, VLS and VSS, differ in particle state and growth rate, for example, but all particle-assisted nanowire growth results confirm that the interfacial energy terms at the growth front are lower, which favors unidirectional growth [127]. The nucleation model can, therefore, be applied for both liquid and solid particles.

Nanowire growth

The recent *in situ* studies have deepened our understanding of nucleus formation by providing further information about the nucleation process. One striking observation is that the growth of nanowires occurs in a regular time scale in which an "incubation time" is required for each step to reach the critical supersaturation and to form the nucleus [126]. A rapid step flow forms a monolayer immediately after the nucleus has formed. The growth subsequently pauses (the incubation time) until the catalyst particles have been refilled with material. Nanowire growth continues in this manner, with regular nucleation followed by the step flow, as long as the supply of material is maintained.

5.1.2. Polytypism

The crystal structure of bulk III-V materials at equilibrium is ZB, except for the nitride-based materials, where it is WZ. The crystal structure of III-V nanowires, in contrast, can be tuned from the ZB to the WZ structure (Section 2.1) [133, 134]. In fact, grown nanowires often contain undesired stacking faults, twin planes and/or a mixture of the ZB-WZ crystal structures. These undesired crystal imperfections adversely affect the electrical and optical properties of the nanowires by, for example, changing the band gap or reducing the carrier mobility [12, 135-137]. On the other hand, this polytypic nature of nanowires allows for the formation of materials with engineered crystal structures, which is not possible in the bulk material.

Nanowires grow in a layer-by-layer fashion, initiated by the formation of a nucleus. The properties of the nucleus, therefore, determine the crystal structure. This means that the parameters that affect nucleus formation also affect the crystal structure [128, 138]. Nanowires grow in a complex dynamic process in which several processes, such as oscillatory nucleus formation, and changes in the surface energy and interface energy, take place simultaneously. These processes all affect the crystal structure [35, 126]. Fluctuations in the supply of materials and thermal fluctuations that occur during the nanowire growth process also affect the crystal structure [139, 140].

The processes and parameters that control the crystal structure of nanowires have not been investigated in the work presented here. However, the different structures that can be formed were used as templates in Papers IV and V.

5.1.3. Mass transport

Material supplied to the nanowire growth process can follow several pathways, including (1) direct impingement onto the catalyst particles, (2) desorption from the catalyst particle, (3) diffusion from the nanowire side facets to the catalyst particle, (4) desorption from the side facets, (5) diffusion from the substrate to the side facets, (6) diffusion along the side facets to the catalyst particle, and (7) nucleation on the

substrate surface (Figure 5.4) [141]. Diffusion of the materials supplied (hereafter known as "adatoms") plays a significant role in the nanowire growth process. In general, Group III adatoms are much more mobile than Group V adatoms, and growth occurs with an excess of the Group V precursor (except in the case of Sb-based nanowires). This section describes the effect of diffusion on the growth behavior of nanowires.

The surface diffusion length of an adatom determines the size of a collection area on the substrate around each nanowire. Material is supplied from this collection area during the growth process. As the nanowire growth continues and the nanowire length exceeds the diffusion length, adatoms diffusing from the substrate cannot reach the catalyst particle. Growth has now reached a steady state. The mass transport-limited model describes the effect of diffusion on the growth of nanowires and shows that the rate depends on $1/r$, where r is the nanowire radius [141, 142].

Paper II describes investigations into the epitaxial growth of InAs nanowires on an InAs buffer layer grown on a Si (111) substrate (Section 4.2.2), during which the inverse relationship between the nanowire length and its diameter was observed.
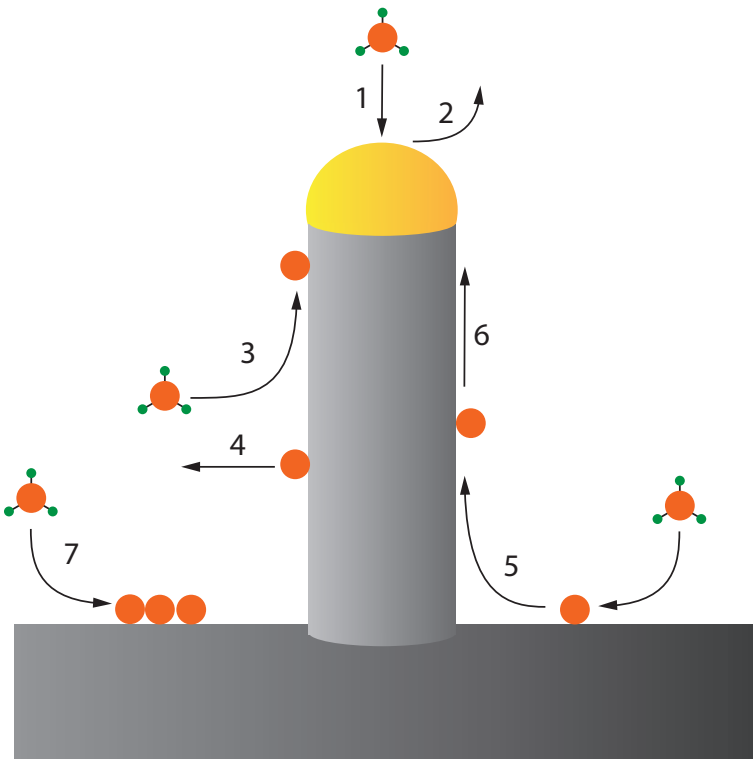

Figure 5.4 Mass transport model for the nanowire growth process, showing various pathways by which material can contribute to the growth process. This drawing is a simplified illustration, and shows completely decomposed precursors on the nanowire side facets and substrate surface.

Nanowire growth

Temperature affects the nanowire growth process in several ways. (i) Nanowires grow in a kinetics-limited growth regime in which pyrolysis of the precursors is incomplete, as described in Section 2.3. Increasing the temperature thus provides more material for the nanowire growth, and this may increase the nanowire growth rate [143]. (ii) Both diffusion and desorption are thermally activated processes, and increasing the temperature affects both the diffusion length and desorption rate of the adatoms. (iii) A change in temperature may affect the solubility of adatoms in nanoparticles. Therefore, the temperature has complicated and interrelated effects on the nanowire growth.

5.1.4. The Gibbs Thomson effect

The mass transport-limited model assumes that supersaturation inside the catalyst particles is high, which means that the model cannot be applied when small catalyst particles are used. This section discusses the growth behavior of small catalyst particles with low supersaturation.

The mass transport-limited model states that the rate of growth is inversely proportional to the diameter of the catalyst particle. In other words, nanowires seeded by small catalyst particles grow faster than those seeded with large particles. Givargizov *et al.* [144], however, observed that there is a critical diameter below which Au-seeded Si whiskers do not grow. This is due to what is known as the "Gibbs Thomson effect", in which a decrease in the catalyst size lowers the supersaturation, due to the higher vapor pressure of the small particles. Equation 5.3 relates the reduction of the supersaturation to particle size,

$$\Delta\mu = \Delta\mu_0 - \frac{4\gamma\Omega}{D} \tag{5.3}$$

where $\Delta\mu$ is the supersaturation of growth species inside the alloy particles (for example Si inside Au-Si alloy particle with respect to the vapor phase), $\Delta\mu_0$ is the supersaturation in the bulk material, and D is the nanowire diameter, and can be assumed to approach infinity in the bulk material. γ is the free energy of the nanowire surface and Ω is atomic volume of growth species inside the alloy particles (Si in the Au-Si particle).

Introducing the particle supersaturation (the partial pressure ratio shown in Equation 2.4) into Equation 5.3 and using radius r (instead of the diameter) gives Equation 5.4:

$$k_B T \, \ln\frac{p_r}{p^\infty} = \mu_l^r - \mu_l^\infty = \frac{2\gamma\Omega}{r} \tag{5.4}$$

where k_B is Boltzmann constant and T is absolute temperature. $\frac{p_r}{p^\infty}$ is the catalyst particle supersaturation expressed as the partial pressure ratio. μ_l^r and μ_l^∞ are the

chemical potentials inside the liquid particle and the bulk material, respectively. Simplifying Equation 5.4 gives the radius-dependent vapor pressure (p_r), shown in Equation 5.5:

$$p_r = p^\infty \exp\left(\frac{2\gamma\Omega}{rk_BT}\right) \tag{5.5}$$

where p^∞ is the vapor pressure of the bulk material. Fröberg *et al.* [145] optimized the calculation of the rate of growth of nanowires from the mass transport-limited model by adding the Gibbs Thomson effect.

Paper VI describes experiments in which the growth rate of $Ga_xIn_{1-x}Sb$ nanowires increased with diameter. We explained this growth behavior based on the Gibbs Thomson effect. Figures 5.5a-e are SEM images of a set of InAs-InSb-$Ga_xIn_{1-x}Sb$ nanowires seeded with Au nanoparticles with diameters of 30-70 nm. The purple overlay shows the $Ga_xIn_{1-x}Sb$ segment, which scales directly with the Au nanoparticle diameter.

Figure 5.5f shows the $Ga_xIn_{1-x}Sb$ growth rate as a function of nanowire diameter for three sets of samples grown with different TMSb molar fractions and Ga/In ratios. The solid curve has been fitted to the black data points based on the Gibbs Thomson model. $Ga_xIn_{1-x}Sb$ is a ternary material, and thus we assumed Raoult's law is valid.

This enabled us to replace p^∞ with xp_v^*, where x is the fraction of Sb in the Au alloy ($x = 0.01$) and p_v^* is the saturation vapor pressure of pure Sb.

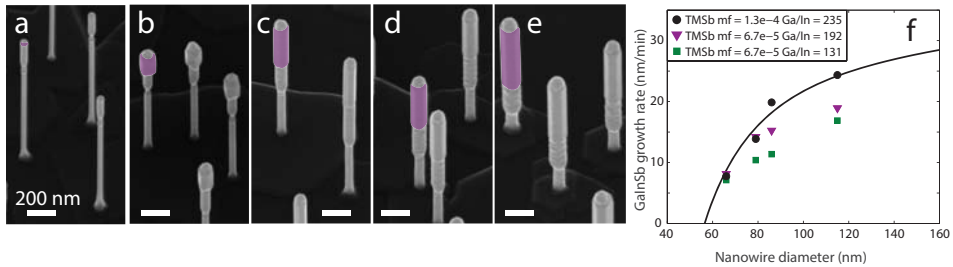**Figure 5.5** (a-e) 30° tilted SEM images of InAs-InSb-$Ga_xIn_{1-x}Sb$ nanowires grown with Au nanoparticles of diameter 30, 40, 50, 60, and 70 nm, respectively. The purple overlay highlights the top $Ga_xIn_{1-x}Sb$ segment, and shows the effect of the Gibbs Thomson effect. These samples were grown with a TMSb molar fraction of 6.72×10^{-5} and a Ga/In ratio of 192, and correspond to the purple data points shown in Figure 5.5f. (f) Rate of growth of $Ga_xIn_{1-x}Sb$ nanowires as a function of the nanowire-particle diameter (measured after the growth had occurred, corresponding to nominal Au diameters of 40, 50, 60, and 70 nm) for three sets of samples grown under different conditions. The solid curve shows a fit to the black data points based on the Gibbs Thomson model. The figure has been adapted from Paper VI.

5.1.5. Reservoir effect

Heteroepitaxial growth of nanowires enables various materials with interesting properties to be combined. In particular, the axial heteroepitaxial growth of nanowires is highly important in many devices [19, 146, 147]. However, the use of catalyst seed particles makes the controlled growth of these nanowires difficult, and properties such as interface sharpness are difficult to control. Section 5.1.1 has described how the catalyst seed particle forms an alloy with Group III or Group IV elements. It is generally assumed that the Group V elements (except Sb) do not dissolve in the Au nanoparticles, and this assumption is supported by post-growth particle analysis. *Ex situ* particle analysis has confirmed that Group III atoms in III-V nanowires remain in the Au nanoparticles even after growth.

If we consider the Au-seeded growth of a Si-Ge axial heterostructure, a definite number of Si atoms are available inside the liquid Au nanoparticles at the beginning of the Ge segment growth. As the nanoparticles are refilled with Ge atoms, the residual Si atoms rapidly mix with the newly incorporated Ge atoms and gradually leave the nanoparticles to be incorporated into the growth. This causes a gradual decrease in the concentration of Si atoms in the liquid Au nanoparticles, which causes a graded Si-Ge transition region to form. This graded interface (which arises as a result of what is called the "reservoir effect") is one of the main challenges in the axial heteroepitaxial growth of catalyst-seeded nanowires [148, 149].

The axial growth of heteroepitaxial nanowires with dissimilar Group III elements can result in a graded interface, as the remaining atoms of the Group III elements are gradually emptied out from the Au nanoparticle. The interface sharpness is governed by the affinity of Au for the corresponding Group III elements. Au has higher affinity for In than Ga, which results in a sharp interface for a switch from Ga to In, and a graded interface for a switch in the opposite direction [150, 151]. Paper III describes studies of the interface properties of InSb-GaSb axial nanowires grown in both directions.

Figure 5.6a shows XEDS line scans overlaid onto a STEM HAADF image of the GaSb-InSb nanowire, while Figure 5.6b shows the reversed structure. The white arrows indicate the growth direction. The interface from the GaSb to InSb segment is sharp, while in the opposite direction it is graded. The length of the gradient is about 50 nm, and the composition stabilizes at $Ga_{0.6}In_{0.4}Sb$. Antimonide-based nanowires have significantly more Sb in the particle than other Group V elements, but these results confirm that the interface sharpness is still governed by the Au affinity for the Group III elements, even in the presence of Sb.
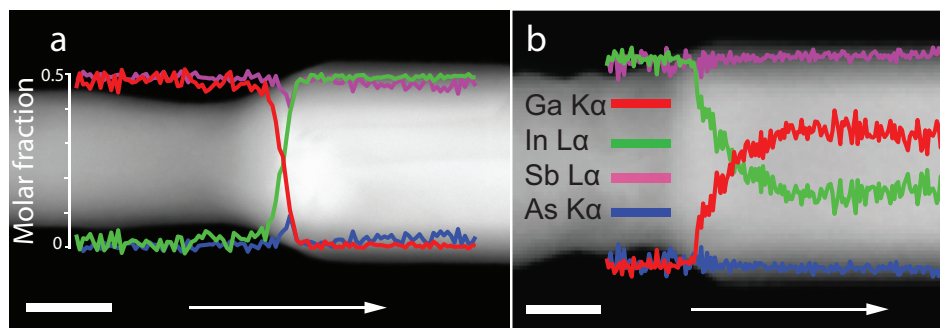
Figure 5.6 XEDS line scans and STEM HAADF images for (a) a 50 nm Au-seeded GaAs-GaSb-InSb nanowire, and (b) a 60 nm Au-seeded InAs-InSb-GaSb nanowire. The red, green, magenta and blue signals correspond to Ga, In, Sb and As, respectively. The interface from GaSb to InSb is sharp, while it is graded in the opposite direction. Scale bar is 50 nm. The figure has been adapted from Paper III.

Post-growth analysis provides valuable information about trends in the composition of the particle, and has shown that Sb affects the solubility of Group III elements in the particles (Paper III).

The sharp interface from GaSb to InSb suggests that there is an incubation time required for the InSb segment since a minimum amount of In is required before the growth. The graded interface in the opposite direction, together with the low amount of Ga (~4%) in the particle even after 30 min growth, suggests that it is not necessary to reach a high level of Ga (incubation time) to initiate the GaSb growth. This is discussed in detail in Paper III.

5.2. Antimonide-based nanowires

The epitaxial growth of antimonide-based nanowires differs significantly from that of arsenide and phosphide materials such as InAs and InP. This section investigates challenges for the growth of antimonide-based nanowires.

One of the main challenges for antimonide-based growth arises due to the fact that the source material is not a hydride. Epitaxial growth of arsenides and phosphides often uses hydride-based Group V precursors (such as arsine (AsH_3) and phosphine (PH_3)). It should be mentioned that Group V sources that are not hydrides, such as tertiary-butyl arsine (TBAs) and tertiary-butyl phosphine (TBP), are available, but these are not commonly used. The hydride-based antimony source (stibine, SbH_3) is unstable and reacts with its container [152]. Trimethylantimony (TMSb) and triethylantimony (TESb) are therefore commonly used as sources of Group V elements. The lack of a stable antimony hydride makes antimonide-based growth more difficult to understand, since the decomposition of these precursors (including

their interactions with Group III precursors) is quite different. Using these precursors may, furthermore, lead to the presence of additional carbon contaminants, and the electrical properties of the nanowires will thus be poorer.

Epitaxial growth of antimonides differs from that of arsenides and phosphides in several other fundamental ways. Two major differences are the low melting point of the antimonide-based compounds [55], and the low equilibrium vapor pressure of elemental antimony [68, 152, 153]. The latter causes excess antimony that lands on the surface and is not incorporated into the growing material to remain on the surface. Antimony has a low solubility in the growing material, which also causes excess antimony to segregate to the surface [68, 153]. Antimony is a well-known surfactant that has been used to alter the surface properties of growing materials. Kimura *et al.* [154], for example, have shown that TESb acts as a surfactant during the growth of GaN-based GaNAs alloys. The low melting point of antimonide compounds limits the temperature window in which growth can take place. The melting point of InSb, for example, is 525 °C, and growth should take place at a temperature below this, where decomposition of the antimony precursor is not complete.

The properties of antimony make it necessary to take special care when growing antimonide-based compounds. Most of the antimonide-based nanowires described in this thesis (except for the GaSb nanowires grown on GaSb layers, Section 5.2.2) were grown after a reactor cleaning step that included a sufficient flow of HCl at high temperature. Proper cleaning ensures that any antimony that remains from the previous run is removed, and enables a systematic study to be carried out without any reactor "memory effect".

5.2.1. Miscibility gap

Several ternary antimonide compounds, such as GaP_xSb_{1-x} and $GaAs_xSb_{1-x}$, are immiscible over a large composition range known as the "miscibility gap" [43, 155]. This section discusses the thermodynamic background to the miscibility gap.

Consider the ternary compound $GaAs_xSb_{1-x}$, which is composed of the binary materials GaAs and GaSb (which have a lattice mismatch of 7.8%). The miscibility gap of this compound is particularly large [156]. Equation 5.6 gives the change in the Gibbs free energy that occurs when the two binary materials are mixed:

$$\Delta G = \Delta H - T\Delta S \tag{5.6}$$

where ΔH is the change in enthalpy of the mixture, ΔS is its change in entropy, and T is the temperature. By considering a model known as the "regular solution model" (RSM), the enthalpy of the mixture could be written, as shown in Equation 5.7,

$$\Delta H = \Omega_i X_{GaAs} X_{GaSb} \tag{5.7}$$

where Ω_i is the interaction parameter, which depends on the bond energies. The interaction parameter can vary over the entire range of composition and the RSM is thus based on a simplified assumption. Depending on the interaction parameter value, the ternary compound formation could be favorable or unfavorable (attraction versus repulsion). A miscibility gap arises when the Ω_i value is positive ($\Delta H > 0$), and the phases separate, to give at least two coexisting phases. However, metastable $GaAs_xSb_{1-x}$ layers can be grown in the miscibility gap by selecting a suitable substrate (lattice-matched) and using certain growth conditions [157-159].

Paper V of this thesis describes studies of the epitaxial growth of GaAs-GaAs$_x$Sb$_{1-x}$ core-shell nanowires using MBE, where the Sb content was varied from 10 to ~70%. This covers the range of composition in which miscibility occurs in bulk and thin-film counterparts. The blue circles and red squares in Figure 5.7 show the shell Sb content as a function of shell growth temperature, and show that the Sb content is higher at lower temperatures.

This inverse relationship may be due to the higher Sb desorption at high temperatures, which reduces the Sb that is available for shell growth under otherwise identical growth conditions (precursor molar flows).
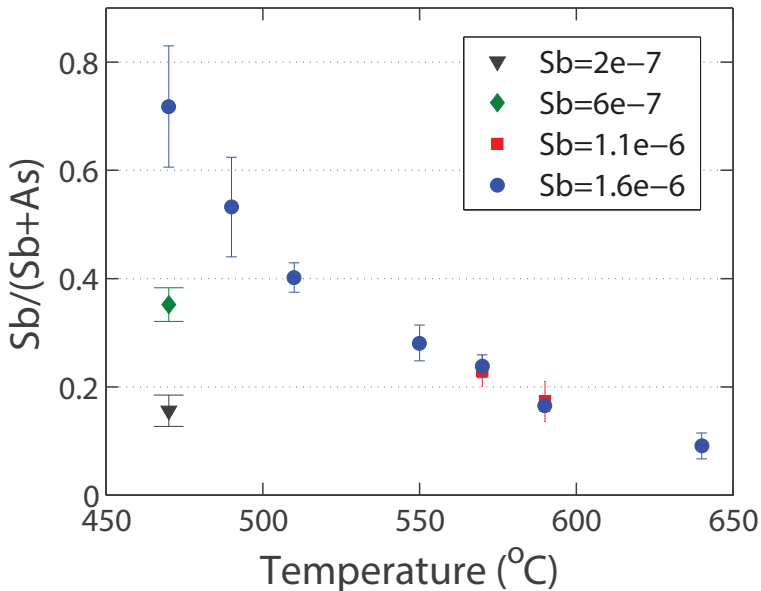

Figure 5.7 The Sb content of the shell (determined by XEDS analysis) for ZB GaAs-GaAs$_x$Sb$_{1-x}$ core-shell nanowires grown at various temperatures between 470 and 640 °C. The blue circles and red squares correspond to Sb fluxes of 1.6×10^{-6} and 1.1×10^{-6} Torr, respectively. The shells have higher contents of Sb at lower temperatures. The filled data points show the average values and the error bars show the standard deviations, averaged over 3-5 nanowires for each sample. The green diamond and black triangle correspond to Sb fluxes of 6×10^{-7} and 2×10^{-7} Torr, respectively, and show that shells of lower Sb content form at lower Sb fluxes. The figure has been adapted from Paper V.

5.2.2. Substrate selection

Selecting a suitable substrate is another challenge when growing antimonide-based nanowires. InSb and GaSb substrates are commercially available, but the surface preparation steps include the removal of native oxide, and are rather difficult (see Section 4.1). Furthermore, direct nucleation of Au-seeded GaSb nanowires on GaAs substrates suffers from improper nucleation, due to the decreased particle contact angle between the particle and the substrate [155].

Paper I describes investigations into the epitaxial growth of Au-seeded GaSb nanowires on as-grown GaSb epitaxial layers (Section 4.2.3). Figure 5.8a shows the system studied. We studied in particular the effects of temperature and the molar fraction of the precursors on nanowire nucleation. No annealing was performed before the nanowires grew.

Changing the temperature and the molar fraction of the precursors showed that the nanowire growth usually failed at the nucleation stage. This gave no vertical nanowire growth. Figure 5.8b is an SEM image of a sample grown at 530 °C, which shows some growth around the Au nanoparticles. It was possible to nucleate some GaSb nanowires at certain growth conditions, although the yield was low (Figures 5.8c-d). Increasing the molar fractions of the precursors (TMGa and TMSb) while keeping the same V/III ratio (3.2) improved the yield. However, high molar fractions of precursor also favored the radial growth of nanowires.

The problems encountered when growing antimonide nanowires on a substrate have led to the use of other III-V nanowires, such as InAs and GaAs, as stems on which to grow these materials. The use of other III-V nanowires as stems limits the temperature that can be used, since the stem may decompose during antimonide growth.
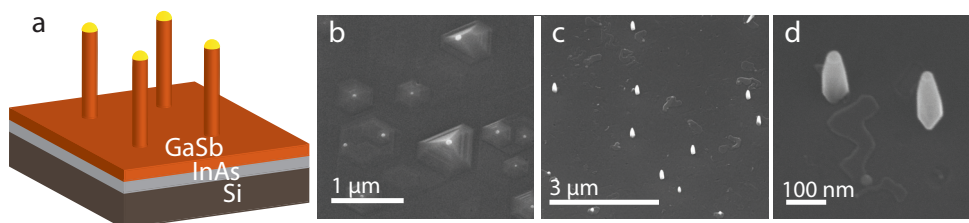

Figure 5.8 (a) GaSb nanowires grown on a GaSb-InAs-Si (111) substrate. (b) 30° tilted SEM image of an attempt to grow GaSb nanowires at 530 °C for 40 min. (c-d) 30° tilted SEM image of GaSb nanowires grown at 420 °C for 30 min with TMGa at a molar fraction of 2.13×10^{-5} and with TMSb at a molar fraction of 6.84×10^{-5} grown at 420 °C for 30 min.

5.3. Complex nanowires structures

The epitaxial growth of III-V binary nanowires has been extensively studied in recent decades for various applications, such as optical and electronic devices [26, 30, 160, 161]. Complex combinations of III-V binary nanowires are required to understand these material systems in more depth and to improve their properties.

Two binary material systems, such as InSb and GaSb nanowires, can be combined in three possible geometries: axial heterostructural growth, radial heterostructural growth, and ternary structures. Figure 5.9a illustrates the axial (InSb-GaSb) geometry and Figure 5.9b illustrates the radial (GaSb-InSb) geometry. Two other geometries are possible, by reversing the order of material stacking along/normal to the growth axis of the nanowire. Figure 5.9c shows the ternary $Ga_xIn_{1-x}Sb$ composition.

Growth aspects of the axial, radial and ternary nanowires will be discussed below.

5.3.1. Axial heterostructures

Axial heteroepitaxial growth of nanowires has emerged as an effective approach to combine various lattice-mismatched material systems, since the small diameter of the nanowires allows effective strain release, which is not possible in planar growth (Section 4.1). The crystal lattices of small-diameter nanowires with small lattice mismatch can deform elastically near the interface and release the strain without defects forming [162-164]. Strain-induced defects and kinks form near the interface when the diameters and lattice mismatch values are large, as is the case for InAs-Si (where the lattice mismatch is approximately 12%) [165, 166]. APDs, however, have never been observed in nanowires [162].
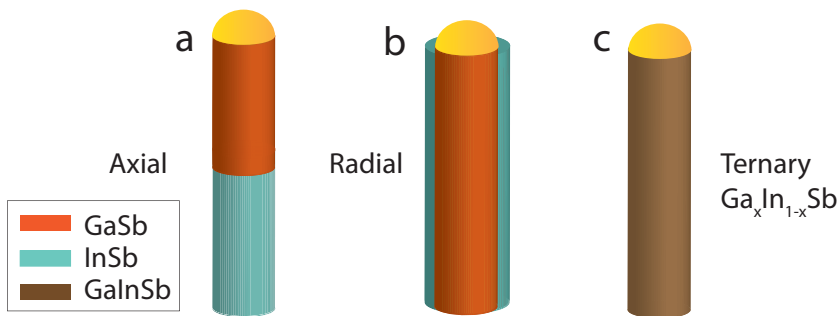

Figure 5.9 (a) Axial and (b) radial heteroepitaxial growth of InSb and GaSb nanowires. (c) $Ga_xIn_{1-x}Sb$ ternary nanowire.

Nanowire growth

This thesis describes studies of the axial heterostructural growth of antimonide-based nanowires (Papers III, VI and VII). A short homoepitaxial stem was initially grown on the substrate material to ensure the proper nucleation of antimonide-based nanowires (Section 5.2.2). The antimonide-based binary segment (a similar Group III-Sb binary material) was subsequently grown. Figures 5.10a-f show schematic illustrations and SEM images of several axial heterostructures in which InAs (GaAs) stems were used, followed by the growth of an InSb (GaSb) segment.

GaAs-GaSb (7.8% lattice mismatch) and InAs-InSb (7% lattice mismatch) are two examples of material systems with rather large lattice mismatches. Figure 5.11 shows HRTEM images of a GaAs-GaSb and an InAs-InSb nanowire interface. The clear contrast along the interfaces (shown by black arrows) indicates the strain that has been induced as a result of the rather large lattice mismatch values. The strain is limited to areas around the interface and does not propagate along the nanowires.

The diameter of the catalyst nanoparticle determines the diameter of the nanowire produced by catalyst-seeded nanowire growth. However, the diameter of InSb and GaSb nanowires always increases in the conditions we have investigated, compared to the similar Group III arsenide and phosphide-based nanowires. The increase in diameter is caused mainly by the uptake of the Group III material, which increases the particle volume and hence increases the nanowire diameter.

In case of the InSb nanowires, post-growth particle analysis shows $AuIn_2$ composition [40, 41, 167]. The orientation of the nanowire side facets differs in the WZ InAs stem from the orientation in the ZB InSb segment [168]. Therefore, looking at the nanowires in <110> direction also magnifies the significant diameter change. It is additionally possible that radial growth on the arsenide stems (either InAs or GaAs) may contribute to the change in diameter. If shell growth occurs on the stem segments, the rate of this growth will be faster on the ZB crystal structure than on the WZ structure (Section 5.3.2). Post-growth particle analysis of particles used in the growth of GaSb nanowires shows that either AuGa or $AuGa_2$ is present, where the composition depends on the molar fraction of TMSb used [38]. Weng *et al.* [169] have shown that the particle composition depends also on the reactor pressure.
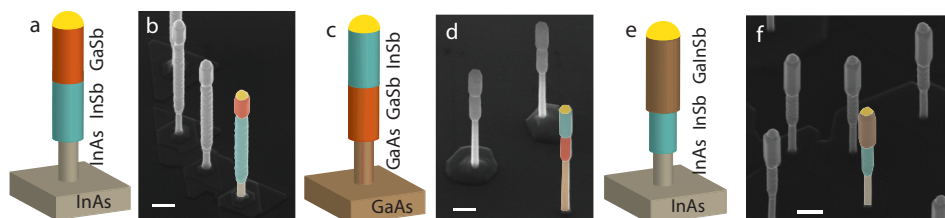

Figure 5.10 Schematic illustrations and 30° tilted SEM images of (a-b) InAs-InSb-GaSb, (c-d) GaAs-GaSb-InSb, and (e-f) InAs-InSb-Ga_xIn_{1-x}Sb nanowires. The diameter increases from the arsenide-based stem material (InAs or GaAs) to the first antimonide-based binary segment (InSb or GaSb). The figure has been adapted from Papers III and VI.
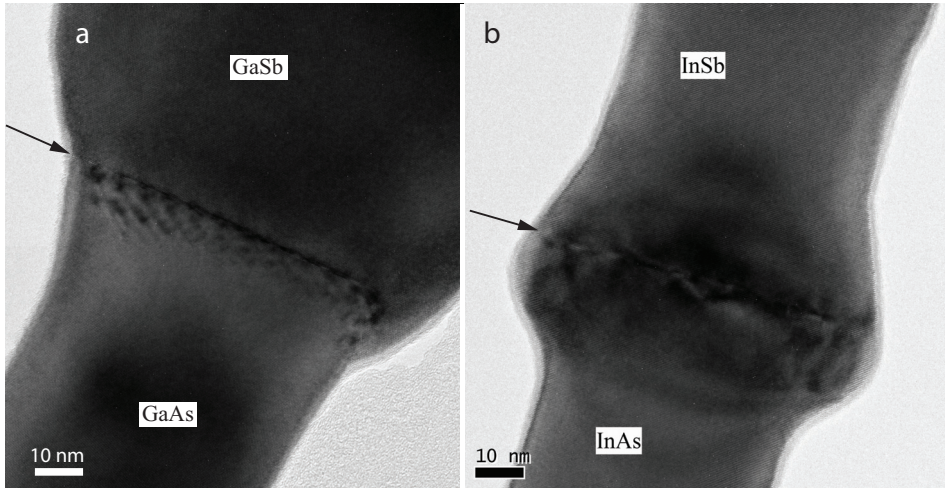
Figure 5.11 HRTEM images of (a) a 60 nm Au-seeded GaAs-GaSb axial heterostructural nanowire, and (b) a 70 nm Au-seeded InAs-InSb axial heterostructural nanowire. The black arrows show the interface position. All segments have pure ZB crystal structure [Courtesy of M. Ek].

This thesis describes investigations into the axial growth of GaSb nanowires on InSb (Figures 5.10a-b), the reversed structure (Figures 5.10c-d), $Ga_xIn_{1-x}Sb$ nanowires on InAs-InSb (Figures 5.10e-f), and the latter nanowires on GaAs-GaSb stems (not shown). The diameter increased significantly from the arsenide-based stem material (InAs or GaAs) to the antimonide-based binary segment (InSb or GaSb).

Figures 5.10b and 5.10d show that the diameter changes from the InSb (GaSb) binary segment to the GaSb (InSb) segment. We attributed this diameter change to radial decomposition of the first antimonide-based binary segment (Paper III). All nanowires were characterized by XEDS analysis, which showed that significant shell growth had not occurred. SEM images of the InAs-InSb-GaSb nanowires showed clearly that microfacets had formed on the InSb stems. The equilibrium shape of a crystal is governed by the chemical potential, and different surface structures are thermodynamically stable at different chemical potentials [102, 103, 170]. The formation of microfacets on the InSb segment can, therefore, be attributed to a change in chemical potential. The molar fraction of TMSb was the same for both antimonide-based binary segments. The diameter of the first antimonide-based binary segment was significantly lower when the second antimonide-based binary segment was allowed to grow for a longer period, and the top part broke off after very long growth periods. This reduction in diameter was more pronounced at the InAs-InSb (GaAs-GaSb) interface, which may be due to the strain induced from the lattice mismatch in this case.

Sets of InAs-InSb and GaAs-GaSb nanowires were grown and were kept under hydrogen for 10 min at the growth temperature (470 °C). Structural characterization

of those samples (not shown) showed that no decomposition or microfacet formation had taken place. We conclude that the decomposition of the InSb (GaSb) takes place through a mechanism in which the Group III element also plays an important role (Paper III).

The diameter of $Ga_xIn_{1-x}Sb$ nanowires grown on an InSb stem also changes, due to the radial growth rate of the $Ga_xIn_{1-x}Sb$ segment being higher than that of the InSb segment (Figure 5.10f and Paper VI). The diameter of $Ga_xIn_{1-x}Sb$ nanowires grown on a GaSb stem, in contrast, did not change significantly (Paper VII).

5.3.2. Radial heterostructures

Radial growth geometry provides an interesting template for both fundamental material studies and studies into radial heterostructural device applications [18, 147, 171]. The study of heterostructural nanowires grown with radial geometry is important to understand the differences in the surface energies of various crystal structures and surface terminations.

Radially grown heterostructural nanowires, also known as "core-shell" nanowires, are formed by first growing a core nanowire, then changing the growth conditions such that they favor deposition of a homogeneous shell (bulk growth) around it. The nanowire side facets become covered by shell material. Thus radial heterostructures are formed in a reaction that takes place on the nanowire side facets (and not at the catalyst particle) [29, 172, 173]. Shell growth proceeds by transfer of material from the vapor phase (precursors) to the solid phase (shell material) in a process that differs from the core nanowire growth mechanisms (both VLS and VSS). Subsequent introduction of different materials allows core-multishell nanowires to be formed. These are interesting as building blocks for various devices, such as photovoltaic devices [174] and light-emitting diodes (LED) [29].

The crystal structure of the core nanowire must be carefully controlled, such that homogeneous and uniform shells can grow around it, since stacking defects can act as nucleation sites and result in inhomogeneous shell growth. Non-uniform shell growth in lattice-mismatched systems causes nanowire bending, due to the strain between the core and shell. Intentional formation of stacking defects in the core nanowire, however, allows quantum dashes and quantum dots (QD) to be formed during the shell growth process [175].

Paper IV describes studies of the epitaxial growth of InP shells around various pure InAs core crystal structures, including WZ, ZB, and {111}-type and {110}-type faceted ZB twin-plane superlattice (TSL) structures. A short axial InP protective segment was initially grown on top of the InAs core nanowires, in order to avoid InAs core nanowires decomposing by an inverse VLS mechanism. The growth rate of the

InP shell was considerably lower on WZ nanowires than it was on ZB nanowires, which suggests that the surface energy of the side facets is lower.

Characterization of the composition of the ZB and TSL nanowires revealed that considerable radial growth occurs around the InAs core nanowires after the top protective InP segment (no intentional shell growth). This growth is attributed to the higher surface energy. The InP shells that grew on two different TSL types were similar. Figures 5.12a and 5.12b are SEM images of the {111}-type TSL nanowires before and after 30 sec of shell growth.
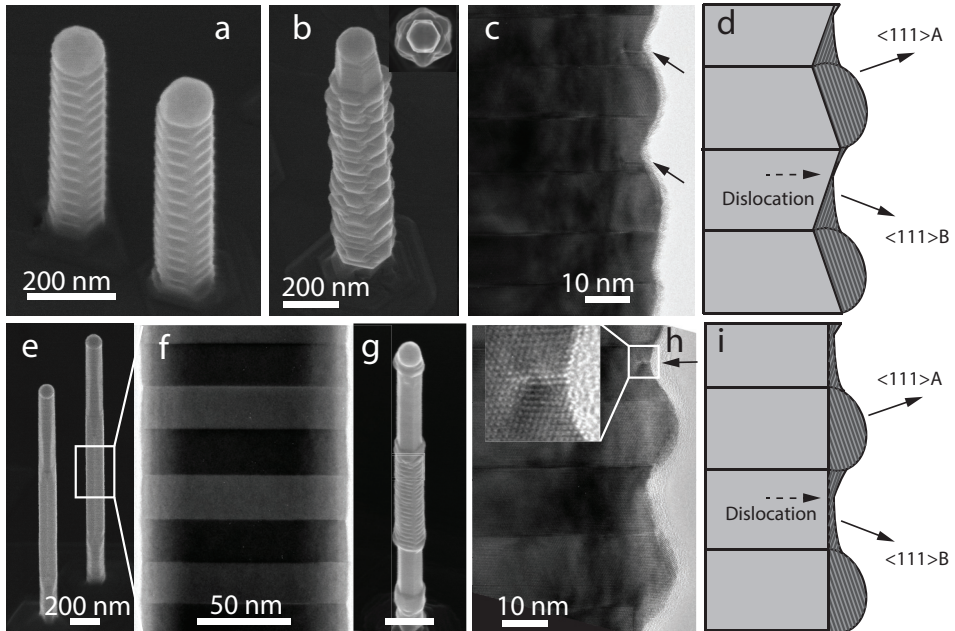
Figure 5.12 30° tilted SEM images of (a) 100 nm diameter Au-seeded InAs {111}-type TSL nanowires without any shell, and (b) 90 nm diameter Au-seeded InAs-InP TSL core-shell nanowires with a shell growth time of 30 sec showing fringed side facets shell growth. The inset shows a top view of the hexagonal cross-sectional TSL nanowire with alternating outwardly directed shell growth. (c) HRTEM image of a TSL nanowire similar to that shown in (b) with only top-protective InP segment growth, showing the initial stage of the shell growth. (e) 30° tilted SEM image of 80 nm diameter Au-seeded InAs {110}-type TSL nanowires without any shell. (f) HRTEM image of a nanowire similar to that shown (e). (g) 30° tilted SEM image of an 80 nm diameter Au-seeded InAs-InP core-shell nanowire after the growth of the top protective InP segment. The scale bar is 200 nm. (h) HRTEM image of a nanowire similar to that shown in (g), showing periodic side facets. (d) Illustration of the InP shell growth on {111}-type TSL nanowires, and (i) on {110}-type TSL nanowires, showing that shell growth is faster in the <111>A direction than in the <111>B direction, where the dashed black arrows show the possible positions of the strain-induced dislocations. The figure has been adapted from Paper IV.

Figure 5.12c is an HRTEM image of a similar TSL nanowire where only the top protective InP segment has grown (no intentional shell growth). Figure 5.12c shows the initial stage of shell growth, and suggests that the growth rate of the shell along the <111>A direction is higher than that along the <111>B direction. Figure 5.12e and g show respective SEM images of the {110}-type TSL nanowires before and after the shell growth (where only the top protective InP segment has grown). Figure 5.12f is an HRTEM image of such a nanowire before the shell growth, while Figure 5.12h shows a nanowire after shell growth. The results confirm that the shell growth behavior is the same for {111}-type and {110}-type TSL nanowires, which is shown in detail in the schematic illustrations, Figures 5.12d and 5.12i. The dashed black arrows in Figures 5.12d and 5.12i show positions at which strain-induced dislocations may form. It should be noted that {110}-type side facets are non-polar and their dangling bonds are anisotropic [176].

Paper V describes studies of the epitaxial growth of the $GaAs_xSb_{1-x}$ shells grown by MBE around GaAs core nanowires. As for InAs-InP core-shell nanowires, the rate of growth of the shell was considerably higher on ZB nanowires than it was on WZ nanowires. Diameter measurements of the samples grown for various shell growth times suggested that the shell growth rate is linear.

5.3.3.   Ternary nanowires

A ternary III-V nanowire is formed when two binary materials with the same Group III or Group V element are combined. If the elements from any one group are different, a quaternary III-V nanowire is formed. The epitaxial growth of ternary nanowires allows two binary materials to be combined, which introduces an additional degree of freedom, "composition tuning", allowing for the control of a physical property (band gap). This section describes the differences between ternary and binary nanowire growth.

The epitaxial growth of ternary nanowires is more complicated than that of binary nanowires. The miscibility gap (Section 5.2.1) is a major challenge when forming some ternary materials and it limits the ways in which the composition can be tuned. Paper V describes investigations into the epitaxial growth of $GaAs-GaAs_xSb_{1-x}$ core-shell nanowires using MBE, where the Sb content was varied from 10 to ~70%. This range encompasses the miscibility gap. Figures 5.13a-e are SEM images of a set of $GaAs-GaAs_xSb_{1-x}$ core-shell nanowires grown by MBE at 470, 510, 550, 570 and 590 °C, respectively. The SEM images show that shell morphology changes considerably with temperature, with the most dramatic change below 550 °C. Nanowires with high Sb content grown at low temperature have an inhomogeneous shell, due to the high lattice mismatch, which favors island-type growth. The formation of the inhomogeneous shells at low temperatures was studied in more detail by lowering the Sb flux (at 470 °C), shown by the green diamond and black triangle in Figure 5.7.

Shell morphology improved significantly when the Sb flux was lowered, and the nanowires formed had an appearance similar to that shown in Figure 5.13e. Lowering the Sb flux affects the migration length of adatoms, but the significant morphology change that occurred shows that shell morphology is governed mainly by strain.

The epitaxial growth of Au-seeded ternary nanowires is more complicated than the growth of binary nanowires. If we consider MOVPE growth of the Au-seeded ternary nanowires, the decomposition pathway of the precursors could be rather different (compared to the growth of binaries), affecting the amount of the available material for the nanowire growth process. The epitaxial growth of ternary nanowires with two Group III elements, such as $Ga_xIn_{1-x}As$, proceeds differently from that of ternary nanowires with two Group V elements, such as $GaAs_xP_{1-x}$. The difference arises from the fact that the solubilities of the Group III elements in the Au nanoparticles are considerably higher than those of the Group V elements. Ternary phase diagrams, for example the Au-Ga-In phase diagram for the Au-seeded $Ga_xIn_{1-x}As$ nanowires, must be studied in order to understand the state of the particle. Guo *et al.* [177] have shown that the composition of Au-seeded $Ga_xIn_{1-x}As$ nanowires grown by MOVPE depends on the composition of the seed particles and on the amount of the supply material.

A serious challenge during ternary nanowire growth is spontaneous phase separation in both axial and radial directions [177-179]. The axial and radial phase separations (for the two Group III ternary nanowires) arise due to the difference in diffusion lengths of the two Group III elements [179, 180], where their diffusion lengths at a given temperature depend also on the substrate/surface atomic structure. In species have longer diffusion lengths than that of Ga adatoms, and thus Ga contributes less to the growth front when the nanowire height exceeds the Ga diffusion length. Ga adatoms are instead deposited on the nanowire side facets.
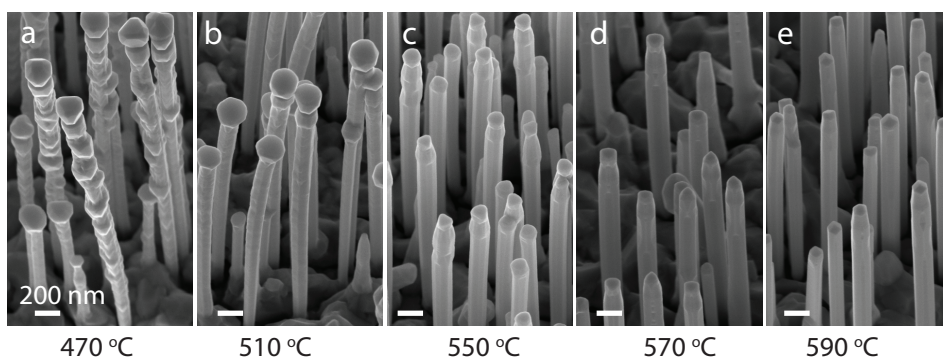

200 nm

470 °C　　510 °C　　550 °C　　570 °C　　590 °C

Figure 5.13 30° tilted SEM images of GaAs-GaAs$_x$Sb$_{1-x}$ core-shell nanowires where the GaAs$_x$Sb$_{1-x}$ shells were grown at (a) 470 °C, (b) 510 °C, (c) 550 °C, (d) 570 °C, and (e) 590 °C with an Sb flux of 1.6 × 10^{-6} Torr. The temperature of the Ga effusion cell was fixed to obtain a nominal planar GaAs growth rate of 0.7 ML s^{-1} on a GaAs (100) substrate, together with an As flux with a beam equivalent pressure of 5.6 × 10^{-6} Torr. The scale bars for (b-e) are 200 nm. Part of the figure has been adapted from Paper V.

This radial growth mechanism is known as "tapering", and it is often inevitable during the nanowire growth process, unless special *in situ* etching steps are carried out [181, 182]. Tapering takes place through a VS growth mode (which is neither VLS nor VSS), and thus the composition of the taper (shell growth) can differ from that of the nanowire itself (core growth).

The epitaxial growth of Au-seeded antimonide-based nanowires with two Group III elements, such as $Ga_xIn_{1-x}Sb$ nanowires, is more challenging than that of arsenide-based or phosphide-based nanowires with two Group III elements, such as $Ga_xIn_{1-x}As$ nanowires, due to the presence of the antimony in the particle. We have demonstrated the growth of $Ga_xIn_{1-x}Sb$ nanowires on both InAs and GaAs substrates for the first time. We have studied the compositions of the particle and the nanowire, and the relationship between them, and have tuned the composition of the nanowires from 3 to 100% In (almost pure GaSb to pure InSb). The post-growth particle analysis of the $Ga_xIn_{1-x}Sb$ nanowires showed that the particles are alloys of Au, In, Ga and Sb, where the composition is determined by the growth conditions. There is little or no post-growth Ga in the particle after the growth of $Ga_xIn_{1-x}As$ nanowires [151], which suggests that the Sb changes the solubilities of the Groups III elements in the particle. The composition of the nanowires followed trends that were similar to those of the composition of the particle, which confirms that the nanowire composition is determined by the corresponding particle composition (Paper VII).

Tuning the composition of the $Ga_xIn_{1-x}Sb$ nanowires showed that the composition is affected by the growth conditions, such as the molar fraction of TMSb and the Ga/In vapor ratio. Figure 5.14a shows the effect of the molar fraction of TMSb on the composition of nanowires (where the Ga/In ratio lies in the solid phase), determined by XEDS analysis. A low molar fraction of Sb favors more Ga-rich nanowires (Paper VI).

The Group III ratios in the vapor and solid phases were clearly correlated (or, in other words, the growth conditions and the nanowire composition were clearly correlated). The Ga/In vapor/solid ratio, however, is surprisingly high (as high as 300). This ratio is considerably higher than that of other ternary nanowires that contain Ga and In, such as $Ga_xIn_{1-x}P$ and $Ga_xIn_{1-x}As$ nanowires, grown at similar temperatures [180, 183-185].

The temperature at which growth occurs has complicated and interrelated effects on the composition and morphology of the nanowires, as briefly mentioned in Section 5.1.3. Paper VII describes extensive studies of the effect of temperature on $Ga_xIn_{1-x}Sb$ nanowires grown on a GaAs substrate. InAs nanowires decompose at high temperatures (which is discussed in Paper IV), and it was not possible to perform similar studies on $Ga_xIn_{1-x}Sb$ nanowires grown on an InAs substrate.
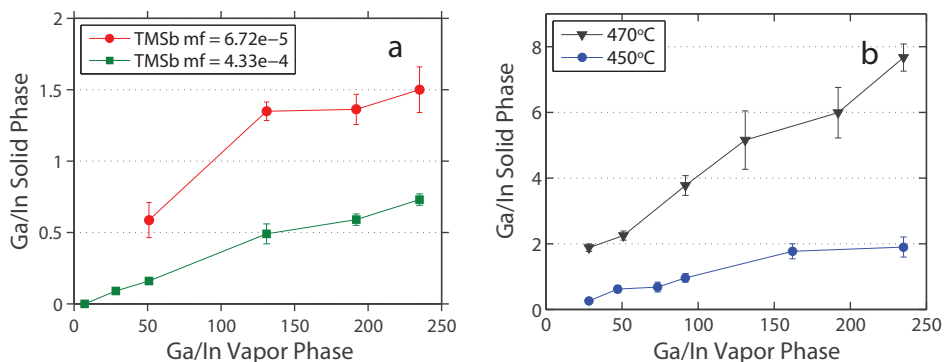
Figure 5.14 The Ga/In ratio of the grown $Ga_xIn_{1-x}Sb$ nanowires (measured by XEDS analysis) as a function of the Ga/In vapor phase ratio (determined by the growth conditions) for (a) $Ga_xIn_{1-x}Sb$ nanowires grown on InAs substrates with two different molar fractions of TMSb, and (b) $Ga_xIn_{1-x}Sb$ nanowires grown on GaAs substrates at two different growth temperatures.

Figure 5.14b shows the effect of temperature on the composition of two sets of samples grown at 450 and 470 °C, and shows clearly that higher temperatures favor more Ga-rich $Ga_xIn_{1-x}Sb$ nanowires (Paper VII).

The temperature study showed also that the nanowire composition is controlled by the kinetics of the decomposition of the precursors, as discussed in Paper VII. We assumed that the two Group III precursors (TMIn and TMGa) decomposed along parallel pathways, and modeled the composition of a set of $Ga_xIn_{1-x}Sb$ nanowires grown under various growth temperatures (450-530 °C). The decomposition of the TMIn precursor was modeled by assuming an Arrhenius-type behavior. It gave a value for the activation energy of 52 kcal/mol and a pre-exponential factor of 4×10^{13} [186].

Temperature affects not only the composition of the nanowire: it affects also the morphology. Less radial growth occurred at high temperature. This may be due to the low decomposition temperature of InSb nanowires, which leads to the competition between radial growth (which occurs by a VS growth mechanism) and nanowire decomposition, depending on the temperature (Paper VII).

All results from experiments in which $Ga_xIn_{1-x}Sb$ nanowires grew confirm that the growth of ternary antimonide-based nanowires is more challenging than the growth of their binary counterparts. Nevertheless, ternary antimonide-based nanowires are an interesting new generation of materials, for which the band gap and carrier mobilities can be precisely tailored for specific applications.

6. Summary and outlook

The results presented here show that it is possible to form promising III-V semiconductor materials into thin layer and nanowire geometries. Several interesting III-V semiconductor materials have been investigated, including InAs, GaAs, InP, InSb, and GaSb. In particular, the epitaxial growth of complex antimonide-based nanowires has been extensively studied. Thin layers and Au-seeded nanowires have been grown using MOVPE, while self-seeded GaAs-GaAs$_x$Sb$_{1-x}$ core-shell nanowires have been grown using the MBE system at NTNU in Trondheim, Norway.

We have successfully integrated high-mobility and direct band gap InAs thin layers and nanowires with Si substrates with a wafer size as large as 2", which confirms that it will be possible to improve the devices, such as FETs, used in applications by combining III-V and Si materials (Papers I and II).

This thesis also describes investigations into combining several III-V semiconductor materials into complex nanowire geometries, including axial and radial heterostructures, and ternary nanowires. It presents results from Au-seeded single and double InSb-GaSb axial heterostructures in both directions, and discusses the composition of the particles and the morphology of the nanowires (Paper III). The work presented here has investigated the radial heteroepitaxial growth of Au-seeded InAs-InP and self-catalyzed GaAs-GaAs$_x$Sb$_{1-x}$, and the results confirm that nanowire morphology and the surface energies are important (Papers IV and V).

The epitaxial growth of ternary nanowires allows nanowires with precise properties, such as composition and band gap, to be formed. We have studied the compositional tuning of GaAs-GaAs$_x$Sb$_{1-x}$ core-shell nanowires (Paper V), and we have demonstrated that Ga$_x$In$_{1-x}$Sb nanowires can be grown by the epitaxial method. We have extensively studied the morphology of the nanowires, and the compositions of the particles and nanowires (Papers VI and VII).

Further work in the study of antimonide-based nanowires will include further investigations into the way in which they form, and will aim to understand, for example, their nucleation and crystal structure. It will be important to understand nucleation and to discover how to nucleate antimonide nanowires directly on a substrate. We have always created a short stem (either InAs or GaAs) on which the antimonide-based structures grow, but this stem may decompose, and lead to problems. It will also be necessary to understand why antimonide nanowires almost always grow in the ZB crystal structure. Radial growth of antimonide nanowires with

the WZ structure may be lower than it is for those with the ZB structure. Furthermore, nanowires with the WZ structure are interesting in studies of fundamental physics.

It is necessary to achieve complex heteroepitaxial growth of a wider variety of materials with antimonide-based materials in the nanowire geometry, in order to form other building blocks that are interesting for many applications. InSb, for example, has the smallest band gap, and the epitaxial growth of a short InSb segment in another wider band gap material may, therefore, be used to form a quantum dot.

Highly controlled complex antimonide-based nanowires with precise properties are required for further developments in applications of devices based on such nanowires. It has been predicted, for example, that $Ga_xIn_{1-x}Sb$ nanowires with tuned compositions have very high electron and hole mobilities, and this property is interesting for high-speed electronics. It will be necessary to study the electrical properties of $Ga_xIn_{1-x}Sb$ nanowires, in order to develop devices based on such nanowires. Further, axial and radial InSb-GaSb heterostructural nanowires with very high electron and hole mobilities are interesting in some devices, such as CMOS devices, in which the combination of n-type and p-type building blocks is required. The epitaxial growth of such structures must be tightly controlled.

Finally, since Au can create mid-gap defects and is incompatible with the Si-based technologies, it will be necessary to investigate the possibility of using other elements for seed particles for the epitaxial growth of III-V semiconductor nanowires.

7. Popular science writing

Nanoscience is the science of understanding and controlling structures at a scale of nanometers in at least one dimension. One nanometer (nm) is equal to one-billionth of a meter. A human hair is approximately 80,000-100,000 nm wide. Nanoscale objects are, of course, invisible to the naked eye. Most viruses have diameters in the range of 20-300 nm, and a single gold atom is one third of 1 nm in diameter. It is interesting to know that our fingernails grow about 1 nm in one second.

Nanoscale materials have dimensions that are much smaller than the dimensions of bulk materials (Figure 1a). Figures 1b-d show two-dimensional (thin layers), one-dimensional (nanowires), and zero-dimensional (nanoparticles) structures.

Nanoscale structures are used in many aspects of our everyday life. One example is sunscreens, which contain nanoparticles to block ultraviolet radiation and protect our skin against sunburn. Another example is electronic devices. The size of such devices has been significantly reduced in recent decades, while their functionality has improved. This has been achieved by reducing the size of the building blocks of our electronic devices. The smallest components now used are nanoscale structures.

The properties of nanoscale materials differ from those of bulk materials. Such materials do not obey classical physics rules. The chemical properties of nanoscale materials differ from those of bulk material. A greater proportion of the object comes in contact with the environment as structures become smaller, and this increase in the surface-to-volume ratio affects the properties of the material. One property that is affected is the reactivity, and nanoscale materials interact more readily than bulk materials.
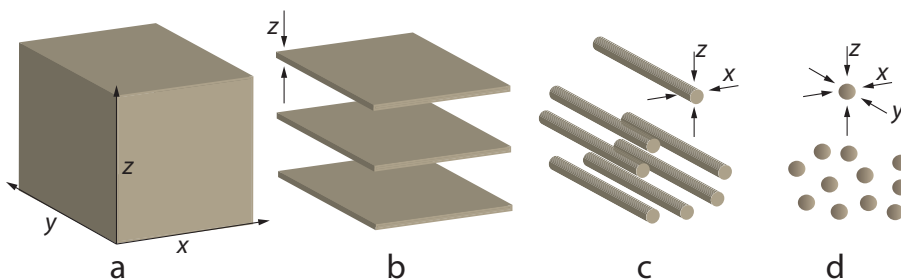

Figure 1 (a) Bulk material, (b) Two-dimensional thin layers, (c) One-dimensional nanowires, and (d) Zero-dimensional nanoparticles.

The work presented in this thesis has studied the synthesis of several compounds of Group III and Group V elements in thin layers (Figure 1b) and nanowires (Figure 1c). These III-V materials are interesting in applications such as electronics and solar cells.

We have synthesized nanostructures through the ordered deposition of atoms to form crystalline materials, in a process known as "epitaxy". The aim of the work was to understand and control the properties of such nanoscale structures and to discover how to combine materials in nanoscale structures that are difficult to combine in bulk structures. We have also examined whether it is possible to combine materials in new ways, to open the door to many new applications. This is one of the most interesting advantages of nanoscale structures.

Some examples of the work presented in thesis are shown in Figures 2a-h. All the images are taken by high-resolution microscopes and their scale bars are 200 nm.
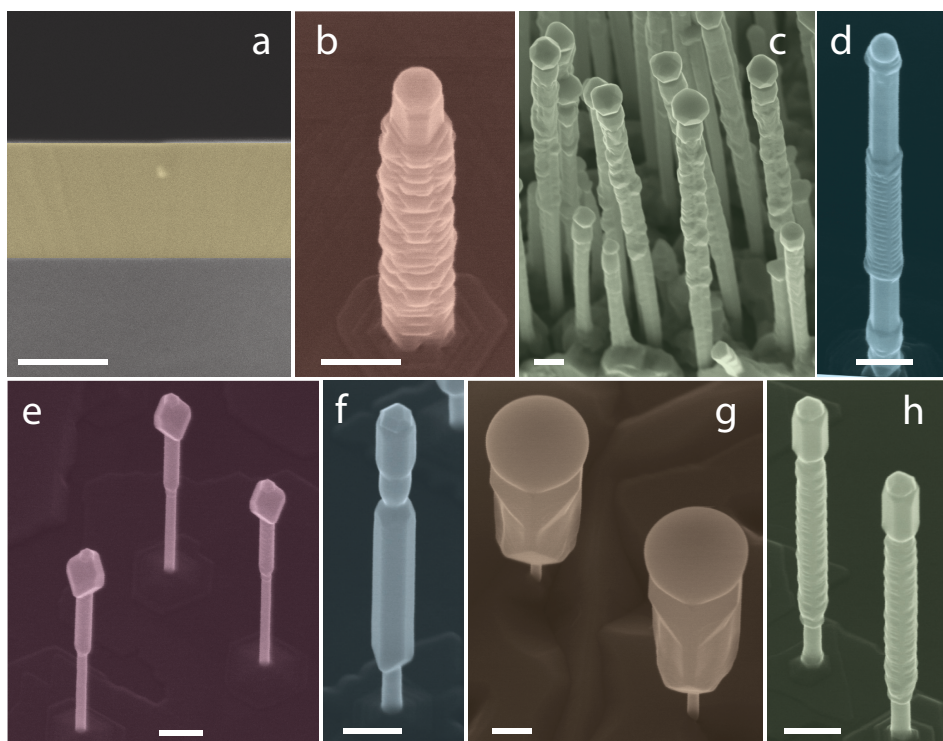

Figure 2 High-resolution images of nanoscale structures created during the work presented in this thesis. (a) Cross-sectional view of a thin layer epitaxially grown on a Si substrates (b)-(h) Nanowire structures formed in various ways and having various compositions.

Nanoscale structures are promising building blocks in many types of application. Understanding and controlling the formation of such structures will allow us to create devices for these applications. Epitaxially grown thin layers are used in several device applications and are commercially available in, for example, certain high-efficiency solar cells. Nanowires with scalable dimensions are interesting candidates for the next generation of electronic devices, which would allow further downscaling of such devices.

8. References

[1]- R. Waser, *Nanoelectronics and Information Technology.* 3rd ed. 2005, Berlin: Wiley-VCH.

[2]- G.M. Whitesides, J.P. Mathias, and C.T. Seto, *Molecular self-assembly and nanochemistry: a chemical strategy for the synthesis of nanostructures.* Science. 1991. **254**: pp. 1312-1319.

[3]- M. Li, H.X. Tang, and M.L. Roukes, *Ultra-sensitive NEMS-based cantilevers for sensing, scanned probe and very high-frequency applications.* Nat. Nanotechnol. 2007. **2**: pp. 114-120.

[4]- A.K. Naik, M.S. Hanay, W.K. Hiebert, X.L. Feng, and M.L. Roukes, *Towards single-molecule nanomechanical mass spectrometry.* Nat. Nanotechnol. 2009. **4**: pp. 445-450.

[5]- F.C. Adams and C. Barbante, *Nanoscience, nanotechnology and spectrometry.* Spectrochimica Acta Part B. 2013. **86**: pp. 3-13.

[6]- I. Vurgaftman, J.R. Meyer, and L.R. Ram-Mohan, *Band parameters for III–V compound semiconductors and their alloys.* J. Appl. Phys. 2001. **89**: pp. 5815.

[7]- R. Chau, S. Datta, M. Doczy, B. Doyle, J. Jin, J. Kavalieros, A. Majumdar, M. Metz, and M. Radosavljevic, *Benchmarking nanotechnology for high-performance and low-power logic transistor applications.* IEEE Trans. Nanotechnol. 2005. **4**: pp. 153-158.

[8]- S.K. Haywood, R.W. Martin, N.J. Mason, R.J. Nicholas, and P.J. Walker, *GaSb/InAs Heterojunctions grown by MOVPE.* J. Cryst. Growth. 1991. **107**: pp. 422-427.

[9]- J. Riikonen, T. Tuomi, A. Lankinen, J. Sormunen, A. Saynatjoki, L. Knuuttila, H. Lipsanen, P.J. McNally, L. O'Reilly, A. Danilewsky, H. Sipila, S. Vaijarvi, D. Lumb, and A. Owens, *Synchrotron X-ray topography study of defects in indium antimonide P-I-N structures grown by metal organic vapour phase epitaxy.* J. Mater. Sci: Mater Electron. 2005. **16**: pp. 449-453.

[10]- Z. Zanolli, F. Fuchs, J. Furthmüller, U. von Barth, and F. Bechstedt, *Model GW band structure of InAs and GaAs in the wurtzite phase.* Phys. Rev. B, 2007. **75**: pp. 245121.

[11]- T. Akiyama, T. Yamashita, K. Nakamura, and T. Ito, *Band alignment tuning in twin-plane superlattices of semiconductor nanowires.* Nano Lett. 2010. **10**: pp. 4614-4618.

[12]- A. De and C.E. Pryor, *Predicted band structures of III-V semiconductors in the wurtzite phase.* Phys. Rev. B. 2010. **81**: pp. 155210.

[13]- F. Dimroth and S. Kurtz, *High-efficiency multijunction solar cells.* MRS Bull. 2007. **32**: pp. 230-235.

[14]- I. Schnitzer, E. Yablonovitch, C. Caneau, T.J. Gmitter, and A. Scherer, *30% external quantum efficiency from surface textured, thin-film light-emitting diodes.* Appl. Phys. Lett. 1993. **63**: pp. 2174.

[15]- S.M. Sze, *Physics of Semiconductor Devices.* 2nd ed. 1981, New York: Wiley.

[16]- J. Wallentin, N. Anttu, D. Asoli, M. Huffman, I. Aberg, M.H. Magnusson, G. Siefer, P. Fuss-Kailuweit, F. Dimroth, B. Witzigmann, H.Q. Xu, L. Samuelson, K. Deppert, and M.T. Borgstrom, *InP nanowire array solar cells achieving 13.8% efficiency by exceeding the ray optics limit.* Science. 2013. **339**: pp. 1057-1060.

[17]- P. Krogstrup, H.I. Jørgensen, M. Heiss, O. Demichel, J.V. Holm, M. Aagesen, J. Nygard, and A. Fontcuberta i Morral, *Single-nanowire solar cells beyond the Shockley–Queisser limit.* Nat. Photonics. 2013. **7**: pp. 306-310.

[18]- A.W. Dey, J. Svensson, M. Ek, E. Lind, C. Thelander, and L.-E. Wernersson, *Combining axial and radial nanowire heterostructures: radial esaki diodes and tunnel field-effect transistors.* Nano Lett. 2013. **13**: pp. 5919-5924.

[19]- A.W. Dey, J. Svensson, B.M. Borg, M. Ek, and L.-E. Wernersson, *Single InAs/GaSb Nanowire Low-Power CMOS Inverter.* Nano Lett. 2012. **12**: pp. 5593-5597.

[20]- J.C. Johnson, H.J. Choi, K.P. Knutsen, R.D. Schaller, P.D. Yang, and R.J. Saykally, *Single gallium nitride nanowire lasers.* Nat. Mater. 2002. **1**: pp. 106-110.

[21]- B. Piccione, C.H. Cho, L.K. van Vugt, and R. Agarwal, *All-optical active switching in individual semiconductor nanowires.* Nat. Nanotechnol. 2012. **7**: pp. 640-645.

[22]- S. Nadj-Perge, S.M. Frolov, E.P. Bakkers, and L.P. Kouwenhoven, *Spin-orbit qubit in a semiconductor nanowire.* Nature. 2010. **468**: pp. 1084-1087.

[23]- V. Mourik, K. Zuo, S.M. Frolov, S.R. Plissard, E. Bakkers, and L.P. Kouwenhoven, *Signatures of Majorana Fermions in Hybrid Superconductor-Semiconductor Nanowire Devices.* Science. 2012. **336**: pp. 1003-1007.

[24]- A. Das, Y. Ronen, Y. Most, Y. Oreg, M. Heiblum, and H. Shtrikman, *Zero-bias peaks and splitting in an Al-InAs nanowire topological superconductor as a signature of Majorana fermions.* Nat. Phys. 2012. **8**: pp. 887-895.

[25]- M.T. Deng, C.L. Yu, G.Y. Huang, M. Larsson, P. Caroff, and H.Q. Xu, *Observation of Majorana Fermions in a Nb-InSb Nanowire-Nb Hybrid Quantum Device.* Nano Lett. 2012. **12**: pp. 6414-6419.

[26]- L.-E. Wernersson, C. Thelander, E. Lind, and L. Samuelson, *III-V Nanowires-Extending a Narrowing Road.* Proc. IEEE, 2010. **98**: pp. 2047-2060.

[27]- X. Jiang, Q. Xiong, S. Nam, F. Qian, Y. Li, and C.M. Lieber, *InAs/InP radial nanowire heterostructures as high electron mobility devices.* Nano Lett. 2007. **7**: pp. 3214-3218.

[28]- J.W.W. van Tilburg, R.E. Algra, W.G.G. Immink, M. Verheijen, E.P.A.M. Bakkers, and L.P. Kouwenhoven, *Surface passivated InAs/InP core/shell nanowires.* Semicond. Sci. Technol. 2010. **25**: pp. 024011.

[19]- F. Qian, S. Gradecak, Y. Li, C.Y. Wen, and C.M. Lieber, *Core/multishell nanowire heterostructures as multicolor, high-efficiency light-emitting diodes.* Nano Lett. 2005. **5**: pp. 2287-2291.

[30]- Y. Li, F. Qian, J. Xiang, and C.M. Lieber, *Nanowire electronic and optoelectronic devices.* Mater. Today 2006. **9**: pp. 18-27.

[31]- P. Caroff, K.A. Dick, J. Johansson, M.E. Messing, K. Deppert, and L. Samuelson, *Controlled polytypic and twin-plane superlattices in III-V nanowires.* Nat. Nanotechnol, 2009. **4**: pp. 50-55.

[32]- J. Bolinsson, P. Caroff, B. Mandl, and K.A. Dick, *Wurtzite-zincblende superlattices in InAs nanowires using a supply interruption method.* Nanotechnology, 2011. **22**: pp. 265606.

[33]- P.K. Mohseni and R.R. LaPierre, *A growth interruption technique for stacking fault-free nanowire superlattices.* Nanotechnology, 2009. **20**: pp. 025610.

[34]- D.L. Dheeraj, G. Patriarche, H. Zhou, T.B. Hoang, A.F. Moses, S. Gronsberg, A.T.J. van Helvoort, B.-O. Fimland, and H. Weman, *Growth and Characterization of Wurtzite GaAs Nanowires with Defect-Free Zinc Blende GaAsSb Inserts.* Nano Lett. 2008. **8**: pp. 4459-4463.

[35]- S. Lehmann, J. Wallentin, D. Jacobsson, K. Deppert, and K.A. Dick, *A general approach for sharp crystal phase switching in InAs, GaAs, InP, and GaP nanowires using only group V flow.* Nano Lett. 2013. **13**: pp. 4099-4105.

[36]- H. Abu-Farsakh and A. Qteish, *Ionicity scale based on the centers of maximally localized Wannier functions.* Phys. Rev. B, 2007. **75**: pp. 085201.

[37]- T. Yamashita, K. Sano, T. Akiyama, K. Nakamura, and T. Ito, *Theoretical investigations on the formation of wurtzite segments in group III–V semiconductor nanowires.* Appl. Surf. Sci. 2008. **254**: pp. 7668-7671.

[38]- M. Jeppsson, K.A. Dick, J.B. Wagner, P. Caroff, K. Deppert, L. Samuelson, and L.-E. Wernersson, *GaAs/GaSb nanowire heterostructures grown by MOVPE.* J. Cryst. Growth. 2008. **310**: pp. 4115-4121.

[39]- B. Mandl, K.A. Dick, D. Kriegner, M. Keplinger, G. Bauer, J. Stangl, and K. Deppert, *Crystal structure control in Au-free self-seeded InSb wire growth.* Nanotechnology, 2011. **22**: pp. 145603.

[40]- D. Ercolani, F. Rossi, A. Li, S. Roddaro, V. Grillo, G. Salviati, F. Beltram, and L. Sorba, *InAs/InSb nanowire heterostructures grown by chemical beam epitaxy.* Nanotechnology, 2009. **20**: pp. 505605.

[41]- P. Caroff, J.B. Wagner, K.A. Dick, H.A. Nilsson, M. Jeppsson, K. Deppert, L. Samuelson, L.R. Wallenberg, and L.E. Wernersson, *High-quality InAs/InSb nanowire heterostructures grown by metal-organic vapor-phase epitaxy.* Small, 2008. **4**: pp. 878-882.

[42]- D.L. Smith, *Thin-film deposition: principles and practice.* 1995, New York: McGraw-Hill.

[43]- G.B. Stringfellow, *Organometallic Vapor-Phase Epitaxy: Theory and Practice.* 2nd ed. 1989, New York: Academic press.

[44]- M.R. Leys, *Fundamental growth kinetics in MOMBE/CBE, MBE and MOVPE.* J. Cryst. Growth. 2000. **209**: pp. 225-231.

[45]- W.T. Tsang, *Advances in MOVPE, MBE, and CBE.* J. Cryst. Growth. 1992. **120**: pp. 1-24.

[46]- M.A. Herman and H. Sitter, *Molecular beam epitaxy-fundamentals and current status.* 2nd ed. 1989, Berlin ; New York : Springer-Verlag.

[47]- G. Biasiol and L. Sorba, *Molecular beam epitaxy: principles andapplications, in Crystal growth of materials for energy production and energy-saving applications*, R. Fornari and L. Sorba, Editors. 2001, Edizioni ETS: Pisa.

[48]- Y. Huang, J.H. Ryou, R.D. Dupuis, V.R. D'Costa, E.H. Steenbergen, J. Fan, Y.H. Zhang, A. Petschke, M. Mandl, and S.L. Chuang, *Epitaxial growth and characterization of InAs/GaSb and InAs/InAsSb type-II superlattices on GaSb substrates by metalorganic chemical vapor deposition for long wavelength infrared photodetectors.* J. Cryst. Growth. 2011. **314**: pp. 92-96.

[49]- R. Rehm, M. Masur, J. Schmitz, V. Daumer, J. Niemasz, T. Vandervelde, D. DeMeo, W. Luppold, M. Wauro, A. Wörl, F. Rutz, R. Scheibner, J. Ziegler, and M. Walther, *InAs/GaSb superlattice infrared detectors.* Infrared Phys. Technol. 2013. **59**: pp. 6-11.

[50]- S.F. Fang, K. Adomi, S. Iyer, H. Morkoc, H. Zabel, C. Choi, and N. Otsuka, *Gallium-arsenide and other compound semiconductors on Silicon.* J. Appl. Phys. 1990. **68**: pp. R31-R58.

[51]- M. Kawabe and T. Ueda, *Self-annihilation of antiphase boundary in GaAs on Si(100) grown by molecular-beam epitaxy.* Jpn. J. Appl. Phys. 1987. **26**: pp. L944-L946.

[52]- S. Jha, X. Song, S.E. Babcock, T.F. Kuech, D. Wheeler, B. Wu, P. Fay, and A. Seabaugh, *Growth of InAs on Si substrates at low temperatures using metalorganic vapor phase epitaxy.* J. Cryst. Growth. 2008. **310**: pp. 4772-4775.

[53]- A. Ishizaka and Y. Shiraki, *Low-temperature surface cleaning of Silicon and its application to Silicon MBE.* J. Electrochem. Soc. 1986. **133**: pp. 666-671.

[54]- W. Kern, *The evolution of Silicon-wafer cleaning technology.* J. Electrochem. Soc. 1990. **137**: pp. 1887-1892.

[55]- M. Yano, H. Yokose, Y. Iwai, and M. Inoue, *Surface-reaction of III-V compound semiconductors irradiated by As and Sb molecular-beams.* J. Cryst. Growth. 1991. **111**: pp. 609-613.

[56]- A.R. Clawson, *Guide to references on III-V semiconductor chemical etching.* Mater. Sci. Eng., R. 2001. **31**: pp. 1-438.

[57]- K. Loschke, G. Kuhn, H.J. Bilz, and G. Leonhardt, *Oxide-films on A(III)B(V) semiconductors.* Thin Solid Films, 1978. **48**: pp. 229-236.

[58]- K. Möller, L. Töben, Z. Kollonitsch, C. Giesen, M. Heuken, F. Willig, and T. Hannappel, *In-situ monitoring and analysis of GaSb(100) substrate deoxidation.* Appl. Surf. Sci. 2005. **242**: pp. 392-398.

[59]- D.A. Allwood, N.J. Mason, and P.J. Walker, *In situ characterisation of MOVPE by surface photoabsorption I. Substrate oxide desorption.* J. Cryst. Growth. 1998. **195**: pp. 163-167.

[60]- J.H. Kang, Q. Gao, H.J. Joyce, H.H. Tan, C. Jagadish, Y. Kim, D.Y. Choi, Y. Guo, H. Xu, J. Zou, M.A. Fickenscher, L.M. Smith, H.E. Jackson, and J.M. Yarrison-Rice, *Novel growth and properties of GaAs nanowires on Si substrates.* Nanotechnology, 2010. **21**: pp. 035604.

[61]- R. DeHoff, *Thermodynamics in materials science.* 1993: New York: McGraw-Hill.

[62]- A.G. Milnes and A.Y. Polyakov, *Gallium antimonide device related properties.* Solid-State Electron. 1993. **36**: pp. 803-818.

[63]- H.M. Manasevit and K.L. Hess, *The use of metalorganics in the preparation of semiconductor-materials.* J. Electrochem. Soc. 1979. **126**: pp. 2031-2033.

[64]- C.B. Cooper, R.R. Saxena, and M.J. Ludowise, *The organometallic VPE growth of GaSb and GaAs$_{1-X}$Sb$_X$ using trimethylantimony.* J. Electron. Mater. 1982. **11**: pp. 1001-1010.

[65]- S.K. Haywood, A.B. Henriques, N.J. Mason, R.J. Nicholas, and P.J. Walker, *Growth of GaSb by MOVPE.* Semicond. Sci. Technol. 1988. **3**: pp. 315-320.

[66]- S.K. Haywood, N.J. Mason, and P.J. Walker, *Growth of GaSb by MOVPE-Optimization of electrical quality with respect to growth-rate, pressure, temperature and III/V ratio.* J. Cryst. Growth. 1988. **93**: pp. 56-61.

[67]- C.A. Wang, S. Salim, K.F. Jensen, and A.C. Jones, *Characteristics of GaSb growth using various gallium and antimony precursors.* J. Cryst. Growth. 1997. **170**: pp. 55-60.

[68]- R.M. Biefeld, *The metal-organic chemical vapor deposition and properties of III-V antimony-based semiconductor materials.* Mater. Sci. Eng., R. 2002. **36**: pp. 105-142.

[69]- M.K. Rathi, B.E. Hawkins, and T.F. Kuech, *Growth behavior of GaSb by metalorganic vapor-phase epitaxy.* J. Cryst. Growth. 2006. **296**: pp. 117-128.

[70]- T. Nguyen, W. Varhue, M. Cross, R. Pino, E. Adams, M. Lavoie, and J. Lee, *Structural evolution and characterization of heteroepitaxial GaSb thin films on Si(111) substrates.* J. Appl. Phys. 2007. **101**: pp. 073707.

[71]- K. Akahane, N. Yamamoto, S.-i. Gozu, and N. Ohtani, *Heteroepitaxial growth of GaSb on Si(001) substrates.* J. Cryst. Growth. 2004. **264**: pp. 21-25.

[72]- K. Akahane, N. Yamamoto, S.-i. Gozu, A. Ueta, and N. Ohtani, *Initial growth stage of GaSb on Si(001) substrates with AlSb initiation layers.* J. Cryst. Growth. 2005. **283**: pp. 297-302.

[73]- H. Toyota, T. Yasuda, T. Endoh, Y. Jinbo, and N. Uchitomi, *Growth and characterization of GaSb heteroepitaxial layers on Si(111) substrates.* Phys. Status Solidi (c), 2008. **5**: pp. 2769-2771.

[74]- G. Balakrishnan, A. Jallipalli, P. Rotella, S. Huang, A. Khoshakhlagh, A. Amtout, S. Krishna, L.R. Dawson, and D.L. Huffaker, *Room-temperature optically pumped (Al)GaSb vertical-cavity surface-emitting laser monolithically grown on an Si(100) substrate.* IEEE J. Sel. Top. Quantum Electron. 2006. **12**: pp. 1636-1641.

[75]- R.J. Malik, J.P. Vanderziel, B.F. Levine, C.G. Bethea, and J. Walker, *Molecular-beam epitaxy of GaSb AlSb optical-device layers on Si(100).* J. Appl. Phys. 1986. **59**: pp. 3909-3911.

[76]- A. Proessdorf, F. Grosse, O. Romanyuk, W. Braun, B. Jenichen, A. Trampert, and H. Riechert, *Interface engineering for improved growth of GaSb on Si(111).* J. Cryst. Growth. 2011. **323**: pp. 401-404.

[77]- A. Subekti, E.M. Goldys, and T.L. Tansley, *Growth of gallium antimonide (GaSb) by metalorganic chemical vapour deposition.* Conf. Optoelectron. Microelectron. Mater. Devices, Proc. ed. C. Jagadish. 1996. pp. 426-429.

[78]- K. Akahane, N. Yamamoto, S.-i. Gozu, A. Ueta, and N. Ohtani, *Residual carrier density in GaSb grown on Si substrates.* Thin Solid Films. 2006. **515**: pp. 748-751.

[79]- G. Astromskas, M. Borg, and L.-E. Wernersson, *Thin InAs membranes and GaSb buffer layers on GaAs(001) substrates.* J. Vac. Sci. Technol. B, 2012. **30**: pp. 051202.

[80]- H. Yuan, S.J. Chua, Z. Miao, J. Dong, and Y. Wang, *Growth and structural properties of thick InAs films on GaAs with low-pressure metalorganic vapor phase epitaxy.* J. Cryst. Growth. 2004. **273**: pp. 63-67.

[81]- H. Ben Naceur, I. Moussa, O. Tottereau, A. Rebey, and B. El Jani, *Heteroepitaxial growth of thin InAs layers on GaAs(100) misoriented substrates: A structural and morphological comparison*. Phys. E. 2009. **41**: pp. 1779-1783.

[82]- S.K. Haywood, R.W. Martin, N.J. Mason, and P.J. Walker, *Growth of InAs by MOVPE- A Comparative study using arsine, tertiarybutylarsine and phenylarsine*. J. Cryst. Growth. 1989. **97**: pp. 489-496.

[83]- H. Naoi, D.M. Shaw, G.J. Collins, and S. Sakai, *Heteroepitaxial growth of InAs by low-pressure metalorganic chemical vapor deposition employing in situ generated arsine radicals*. J. Cryst. Growth. 2000. **219**: pp. 481-484.

[84]- T. Przeslawski, A. Wolkenberg, K. Reginski, J. Kaniewski, and J. Bak-Misiuk, *Growth and transport properties of relaxed epilayers of InAs on GaAs.* Thin Solid Films, 2000. **367**: pp. 232-234.

[85]- H.M. Wang, T.W. Fan, J. Wu, Y.P. Zeng, J.R. Dong, and M.Y. Kong, *Effects of growth temperature on highly mismatched InAs grown on GaAs substrates by MBE.* J. Cryst. Growth. 1998. **186**: pp. 38-42.

[86]- H. Yamaguchi and Y. Horikoshi, *Replacement of group-III atoms on the growing surface during migration-enhanced epitaxy*. J. Appl. Phys. 1990. **68**: pp. 1610-1615.

[87]- C.W. Hsu, Y.F. Chen, and Y.K. Su, *Dislocation reduction of InAs nanofins prepared on Si substrate using metal-organic vapor-phase epitaxy*. Nanoscale Res. Lett. 2012. **7**: pp. 642.

[88]- G.E. Cyrlin, V.N. Petrov, V.G. Dubrovskii, Y.B. Samsonenko, N.K. Polyakov, A.O. Golubok, S.A. Masalov, N.I. Komyak, V.M. Ustinov, A.Y. Egorov, A.R. Kovsh, M.V. Maximov, A.F. Tsatsul'nikov, B.V. Volovik, A.E. Zhukov, P.S. Kop'ev, N.N. Ledentsov, Z.I. Alferov, and D. Bimberg, *Heteroepitaxial growth of InAs on Si: a new type of quantum dot.* Semiconductors, 1999. **33**: pp. 972-975.

[89]- A. Ohtake and K. Mitsuishi, *Polarity controlled InAs{111} films grown on Si(111).* J. Vac. Sci. Technol., B: Microelectron. Nanometer Struct. 2011. **29**: pp. 031804.

[90]- G. Lee and Y.-G. Yoon, *Atomic Structures of a Monolayer of AlAs, GaAs, and InAs on Si(111).* J. Korean Phys. Soc. 2010. **57**: pp. 251-254.

[91]- C.H. Choi, L. Hultman, R. Ai, and S.A. Barnett, *Effect of nucleation mechanism on planar defects in InAs on Si(100).* Appl. Phys. Lett. 1990. **57**: pp. 2931-2933.

[92]- C.H. Choi and S.A. Barnett, *Morphology and crystalline perfection of InAs films on Si(100).* J. Cryst. Growth. 1994. **137**: pp. 381-387.

[93]- C.H. Choi and S.A. Barnett, *Nucleation and epitaxial-growth of InAs on Si(100) by ion-assisted deposition*. Appl. Phys. Lett. 1989. **55**: pp. 2319-2321.

[94]- P. Caroff, M. Jeppsson, D. Wheeler, M. Keplinger, B. Mandl, J. Stangl, A. Seabaugh, G. Bauer, and L.E. Wernersson, *InAs film grown on Si(111) by metal organic vapor phase epitaxy.* J. Phys.: Conf. Ser. 2008. **100**: pp. 042017.

[95]- S. Roddaro, P. Caroff, G. Biasiol, F. Rossi, C. Bocchi, K. Nilsson, L. Froberg, J.B. Wagner, L. Samuelson, L.E. Wernersson, and L. Sorba, *Growth of vertical InAs nanowires on heterostructured substrates.* Nanotechnology, 2009. **20**: pp. 285303.

[96]- M. Lakrimi, R.W. Martin, N.J. Mason, R.J. Nicholas, and P.J. Walker, *GaSb/InAs heterojunctions grown by MOVPE: effect of gas switching sequences on interface quality.* J. Cryst. Growth. 1991. **110**: pp. 677-682.

[97]- H. Kroemer, *The 6.1 angstrom family (InAs, GaSb, AlSb) and its heterostructures: a selective review.* Phys. E. 2004. **20**: pp. 196-203.

[98]- M. Lakrimi, R.W. Martin, N.J. Mason, R.J. Nicholas, and P.J. Walker, *Optimization of the growth by MOVPE of strained GaSb/InAs double heterojunctions and superlattices on [111] GaAs superlattices.* J. Cryst. Growth. 1992. **124**: pp. 395-400.

[99]- B. Satpati, J.B. Rodriguez, A. Trampert, E. Tournié, A. Joullié, and P. Christol, *Interface analysis of InAs/GaSb superlattice grown by MBE.* J. Cryst. Growth. 2007. **301-302**: pp. 889-892.

[100]- B. Brar and D. Leonard, *Spiral growth of GaSb on (001)GaAs using molecular-beam epitaxy.* Appl. Phys. Lett. 1995. **66**: pp. 463-465.

[101]- S.P. Watkins, R. Ares, G. Soerensen, W. Zhong, C.A. Tran, J.E. Bryce, and C.R. Bolognesi, *Atomic force microscopy study of morphology and dislocation structure of InAs and GaSb grown on highly mismatched substrates.* J. Cryst. Growth. 1997. **170**: pp. 788-793.

[102]- N. Moll, A. Kley, E. Pehlke, and M. Scheffler, *GaAs equilibrium crystal shape from first principles.* Phys. Rev. B. 1996. **54**: pp. 8844-8855.

[103]- Q.K.K. Liu, N. Moll, M. Scheffler, and E. Pehlke, *Equilibrium shapes and energies of coherent strained InP islands.* Phys. Rev. B. 1999. **60**: pp. 17008-17015.

[104]- S.A. Fortuna and X. Li, *Metal-catalyzed semiconductor nanowires: a review on the control of growth directions.* Semicond. Sci. Technol. 2010. **25**: pp. 024005.

[105]- Y. Wu, Y. Cui, L. Huynh, C.J. Barrelet, D.C. Bell, and C.M. Lieber, *Controlled growth and structures of molecular-scale silicon nanowires.* Nano Lett. 2004. **4**: pp. 433-436.

[106]- Y. Cui, L.J. Lauhon, M.S. Gudiksen, J. Wang, and C.M. Lieber, *Diameter-controlled synthesis of single-crystal silicon nanowires.* Appl. Phys. Lett. 2001. **78**: pp. 2214.

[107]- J. Wang, S.R. Plissard, M.A. Verheijen, L.F. Feiner, A. Cavalli, and E.P. Bakkers, *Reversible Switching of InP Nanowire Growth Direction by Catalyst Engineering.* Nano Lett. 2013. **13**: pp. 3802-3806.

[108]- S. Kodambaka, J.B. Hannon, R.M. Tromp, and F.M. Ross, *Control of Si nanowire growth by oxygen.* Nano Lett. 2006. **6**: pp. 1292-1296.

[109]- K.A. Dick, *A review of nanowire growth promoted by alloys and non-alloying elements with emphasis on Au-assisted III–V nanowires.* Prog. Cryst. Growth Charact. Mater. 2008. **54**: pp. 138-173.

[110]- K. Hillerich, M.E. Messing, L. Reine Wallenberg, K. Deppert, and K.A. Dick, *Epitaxial InP nanowire growth from Cu seed particles.* J. Cryst. Growth. 2011. **315**: pp. 134-137.

[111]- K. Hillerich, K.A. Dick, M.E. Messing, K. Deppert, and J. Johansson, *Simultaneous growth mechanisms for Cu-seeded InP nanowires.* Nano Res. 2012. **5**: pp. 297-306.

[112]- A.T. Vogel, J. de Boor, M. Becker, J.V. Wittemann, S.L. Mensah, P. Werner, and V. Schmidt, *Ag-assisted CBE growth of ordered InSb nanowire arrays.* Nanotechnology, 2011. **22**: pp. 015605.

[113]- S. Heun, B. Radha, D. Ercolani, G.U. Kulkarni, F. Rossi, V. Grillo, G. Salviati, F. Beltram, and L. Sorba, *Coexistence of vapor-liquid-solid and vapor-solid-solid growth modes in Pd-assisted InAs nanowires.* Small, 2010. **6**: pp. 1935-1941.

[114]- S. Heun, B. Radha, D. Ercolani, G.U. Kulkarni, F. Rossi, V. Grillo, G. Salviati, F. Beltram, and L. Sorba, *Pd-Assisted Growth of InAs Nanowires.* Cryst. Growth Des. 2010. **10**: pp. 4197-4202.

[115]- H. Xu, Y. Wang, Y. Guo, Z. Liao, Q. Gao, H.H. Tan, C. Jagadish, and J. Zou, *Defect-free <110> zinc-blende structured InAs nanowires catalyzed by palladium.* Nano Lett. 2012. **12**: pp. 5744-5749.

[116]- A.C. Ford, J.C. Ho, Z. Fan, O. Ergen, V. Altoe, S. Aloni, H. Razavi, and A. Javey, *Synthesis, contact printing, and device characterization of Ni-catalyzed, crystalline InAs nanowires.* Nano Res. 2008. **1**: pp. 32-39.

[117]- N. Han, F. Wang, A.T. Hui, J.J. Hou, G. Shan, F. Xiu, T. Hung, and J.C. Ho, *Facile synthesis and growth mechanism of Ni-catalyzed GaAs nanowires on non-crystalline substrates.* Nanotechnology, 2011. **22**: pp. 285607.

[118]- Y. Wang, V. Schmidt, S. Senz, and U. Gosele, *Epitaxial growth of silicon nanowires using an aluminium catalyst.* Nat. Nanotechnol. 2006. **1**: pp. 186-189.

[119]- F. Jabeen, M. Piccin, L. Felisari, V. Grillo, G. Bais, S. Rubini, F. Martelli, F. d'Acapito, M. Rovezzi, and F. Boscherini, *Mn-induced growth of InAs nanowires.* J. Vac. Sci. Technol., B: Microelectron. Nanometer Struct. 2010. **28**: pp. 478-483.

[120]- J.L. Lensch-Falk, E.R. Hemesath, F.J. Lopez, and L.J. Lauhon, *Vapor-solid-solid synthesis of Ge nanowires from vapor-phase-deposited manganese germanide seeds.* J. Am. Chem. Soc. 2007. **129**: pp. 10670-10671.

[121]- J.L. Lensch-Falk, E.R. Hemesath, D.E. Perea, and L.J. Lauhon, *Alternative catalysts for VSS growth of silicon and germanium nanowires.* J. Mater. Chem. 2009. **19**: pp. 849-857.

[122]- M.E. Messing, K. Hillerich, J. Bolinsson, K. Storm, J. Johansson, K.A. Dick, and K. Deppert, *A comparative study of the effect of gold seed particle preparation method on nanowire growth.* Nano Res. 2010. **3**: pp. 506-519.

[123]- M.H. Magnusson, K. Deppert, J.-O. Malm, J.-O. Bovin, and L. Samuelson, *Gold nanoparticles: Production, reshaping, and thermal charging.* J. Nanopart. Res. 1999. **1**: pp. 243-251.

[124]- A. Fontcuberta i Morral, *Gold-Free GaAs Nanowire Synthesis and Optical Properties.* IEEE J. Sel. Top. Quantum Electron. 2011. **17**: pp. 819-828.

[125]- R.S. Wagner and W.C. Ellis, *Vapor-Liquid-Solid Mechanism of Single Crystal Growth (New method growth catalysis from impurity whisker epitaxial, and large crystal; E).* Appl. Phys. Lett. 1964. **4**: pp. 89-90.

[126]- F.M. Ross, *Controlling nanowire structures through real time growth studies.* Rep. Prog. Phys. 2010. **73**: pp. 114501.

[127]- B.A. Wacaser, K.A. Dick, J. Johansson, M.T. Borgström, K. Deppert, and L. Samuelson, *Preferential Interface Nucleation: An Expansion of the VLS Growth Mechanism for Nanowires.* Adv. Mater. 2009. **21**: pp. 153-165.

[128]- F. Glas, J.-C. Harmand, and G. Patriarche, *Why Does Wurtzite Form in Nanowires of III-V Zinc Blende Semiconductors?* Phys. Rev. Lett. 2007. **99**: pp. 146101.

[129]- V. Dubrovskii, N. Sibirev, G. Cirlin, J. Harmand, and V. Ustinov, *Theoretical analysis of the vapor-liquid-solid mechanism of nanowire growth during molecular beam epitaxy.* Phys. Rev. E 2006. **73**(2): pp. 021603.

[130]- A.I. Persson, M.W. Larsson, S. Stenstrom, B.J. Ohlsson, L. Samuelson, and L.R. Wallenberg, *Solid-phase diffusion mechanism for GaAs nanowire growth.* Nat. Mater. 2004. **3**: pp. 677-681.

[131]- K.A. Dick, K. Deppert, T. Martensson, B. Mandl, L. Samuelson, and W. Seifert, *Failure of the vapor-liquid-solid mechanism in Au-assisted MOVPE growth of InAs nanowires.* Nano Lett. 2005. **5**: pp. 761-764.

[132]- S. Kodambaka, J. Tersoff, M.C. Reuter, and F.M. Ross, *Germanium nanowire growth below the eutectic temperature.* Science, 2007. **316**: pp. 729-732.

[133]- K. Hiruma, M. Yazawa, T. Katsuyama, K. Ogawa, K. Haraguchi, M. Koguchi, and H. Kakibayashi, *Growth and optical properties of nanometer-scale GaAs and InAs whiskers.* J. Appl. Phys. 1995. **77**: pp. 447.

[134]- J. Johansson, L.S. Karlsson, C.P. Svensson, T. Martensson, B.A. Wacaser, K. Deppert, L. Samuelson, and W. Seifert, *Structural properties of <111>B -oriented III-V nanowires.* Nat. Mater. 2006. **5**: pp. 574-580.

[135]- C. Thelander, P. Caroff, S. Plissard, A.W. Dey, and K.A. Dick, *Effects of crystal phase mixing on the electrical properties of InAs nanowires.* Nano Lett. 2011. **11**: pp. 2424-2429.

[136]- R.L. Woo, R. Xiao, Y. Kobayashi, L. Gao, N. Goel, M.K. Hudait, T.E. Mallouk, and R.F. Hicks, *Effect of Twinning on the Photoluminescence and Photoelectrochemical Properties of Indium Phosphide Nanowires Grown on Silicon (111).* Nano Lett. 2008. **8**: pp. 4664-4669.

[137]- F. Bechstedt and A. Belabbes, *Structure, energetics, and electronic states of III-V compound polytypes.* J. Phys.: Condens. Matter, 2013. **25**: pp. 273201.

[138]- V.G. Dubrovskii and N.V. Sibirev, *Growth thermodynamics of nanowires and its application to polytypism of zinc blende III-V nanowires.* Phys. Rev. B. 2008. **77**(3): pp. 035414.

[139]- J. Johansson, L.S. Karlsson, C.P.T. Svensson, T. Mårtensson, B.A. Wacaser, K. Deppert, L. Samuelson, and W. Seifert, *The structure of <111>B oriented GaP nanowires.* J. Cryst. Growth. 2007. **298**: pp. 635-639.

[140]- Y.C. Chou, K. Hillerich, J. Tersoff, M.C. Reuter, K.A. Dick, and F.M. Ross, *Atomic-Scale Variability and Control of III-V Nanowire Growth Kinetics.* Science, 2014. **343**: pp. 281-284.

[141]- V.G. Dubrovskii and N.V. Sibirev, *General form of the dependences of nanowire growth rate on the nanowire radius.* J. Cryst. Growth. 2007. **304**: pp. 504-513.

[142]- J. Johansson, C.P.T. Svensson, T. Martensson, L. Samuelson, and W. Seifert, *Mass transport model for semiconductor nanowire growth.* J. Phys. Chem. B. 2005. **109**: pp. 13567-13571.

[143]- K.A. Dick, K. Deppert, L.S. Karlsson, L.R. Wallenberg, L. Samuelson, and W. Seifert, *A new understanding of au-assisted growth of III-V semiconductor nanowires.* Adv. Funct. Mater. 2005. **15**: pp. 1603-1610.

[144]- E.I. Givargizov, *Fundamental aspects of VLS growth.* J. Cryst. Growth. 1975. **31**: pp. 20-30.

[145]- L. Fröberg, W. Seifert, and J. Johansson, *Diameter-dependent growth rate of InAs nanowires.* Phys. Rev. B, 2007. **76**: pp. 153401.

[146]- A.W. Dey, B.M. Borg, B. Ganjipour, M. Ek, K.A. Dick, E. Lind, C. Thelander, and L.-E. Wernersson, *High-Current GaSb/InAs(Sb) Nanowire Tunnel Field-Effect Transistors.* IEEE Electron Device Lett. 2013. **34**: pp. 211-213.

[147]- B. Ganjipour, A.W. Dey, B.M. Borg, M. Ek, M.E. Pistol, K.A. Dick, L.E. Wernersson, and C. Thelander, *High current density Esaki tunnel diodes based on GaSb-InAsSb heterostructure nanowires.* Nano Lett. 2011. **11**: pp. 4222-4226.

[148]- N. Li, T.Y. Tan, and U. Gösele, *Transition region width of nanowire hetero- and pn-junctions grown using vapor-liquid-solid processes.* Appl. Phys. A. 2008. **90**: pp. 591-596.

[149]- T.E. Clark, P. Nimmatoori, K.-K. Lew, L. Pan, J.M. Redwing, and E.C. Dickey, *Diameter dependent growth rate and interfacial abruptness in vapor-liquid-solid Si/Si$_{1-x}$Ge$_x$ heterostructure nanowires.* Nano Lett. 2008. **8**: pp. 1246-1252.

[150]- P. Krogstrup, J. Yamasaki, C.B. Sorensen, E. Johnson, J.B. Wagner, R. Pennington, M. Aagesen, N. Tanaka, and J. Nygard, *Junctions in Axial III-V Heterostructure Nanowires Obtained via an Interchange of Group III Elements.* Nano Lett. 2009. **9**: pp. 3689-3693.

[151]- K.A. Dick, J. Bolinsson, B.M. Borg, and J. Johansson, *Controlling the abruptness of axial heterojunctions in III-V nanowires: beyond the reservoir effect.* Nano Lett. 2012. **12**: pp. 3200-3206.

[152]- A. Aardvark, N.J. Mason, and P.J. Walker, *The growth of antimonides by MOVPE.* Prog. Cryst. Growth Charact. Mater. 1997. **35**: pp. 207-241.

[153]- F. Dimroth, C. Agert, and A.W. Bett, *Growth of Sb-based materials by MOVPE.* J. Cryst. Growth. 2003. **248**: pp. 265-273.

[154]- A. Kimura, Z. Liu, and T.F. Kuech, *Antimony as a surfactant during the growth of GaN-based GaNAs alloys by metal organic vapor-phase epitaxy.* J. Cryst. Growth. 2004. **272**: pp. 432-437.

[155]- B. Mattias Borg and L.E. Wernersson, *Synthesis and properties of antimonide nanowires.* Nanotechnology, 2013. **24**: pp. 202001.

[156]- J.B. Li, W. Zhang, C. Li, and Z. Du, *A thermodynamic assessment of the Ga-As-Sb system.* J. Phase Equilib. 1998. **19**: pp. 466-472.

[157]- J. Shin, T.C. Hsu, Y. Hsu, and G.B. Stringfellow, *OMVPE growth of metastable GaAsSb and GaInAsSb alloys using TBAs and TBDMSb.* J. Cryst. Growth. 1997. **179**: pp. 1-9.

[158]- K.D. Moiseev, V.V. Romanov, T.I. Voronina, T.S. Lagunova, M.P. Mikhailova, and Y.P. Yakovlev, *Type II GaAs$_x$Sb$_{1-x}$/InAs (x<0.35) heterojunction grown by MOVPE near a miscibility gap of the ternary solid solution.* J. Cryst. Growth. 2008. **310**: pp. 4846-4849.

[159]- M. Peter, N. Herres, F. Fuchs, K. Winkler, K.H. Bachem, and J. Wagner, *Band gaps and band offsets in strained GaAs$_{1-y}$Sb$_y$ on InP grown by metalorganic chemical vapor deposition.* Appl. Phys. Lett. 1999. **74**: pp. 410.

[160]- H.J. Joyce, Q. Gao, H. Hoe Tan, C. Jagadish, Y. Kim, J. Zou, L.M. Smith, H.E. Jackson, J.M. Yarrison-Rice, P. Parkinson, and M.B. Johnston, *III-V semiconductor nanowires for optoelectronic device applications.* Prog. Quantum Electron. 2011. **35**: pp. 23-75.

[161]- S.A. Dayeh, C. Soci, X.-Y. Bao, and D. Wang, *Advances in the synthesis of InAs and GaAs nanowires for electronic applications.* Nano Today, 2009. **4**: pp. 347-358.

[162]- E. P. A. M Bakkers, M.T. Borgstrom, and M.A. Verheijen, *Epitaxial growth of III-V nanowires on group IV substrates.* MRS Bull. 2007. **32**: pp. 117-122.

[163]- M.T. Bjork, B.J. Ohlsson, T. Sass, A.I. Persson, C. Thelander, M.H. Magnusson, K. Deppert, L.R. Wallenberg, and L. Samuelson, *One-dimensional steeplechase for electrons realized.* Nano Lett. 2002. **2**: pp. 87-89.

[164]- M.W. Larsson, J.B. Wagner, M. Wallin, P. Håkansson, L.E. Fröberg, L. Samuelson, and L.R. Wallenberg, *Strain mapping in free-standing heterostructured wurtzite InAs/InP nanowires.* Nanotechnology, 2007. **18**: pp. 015504.

[165]- K. Tomioka, J. Motohisa, S. Hara, and T. Fukui, *Control of InAs nanowire growth directions on Si.* Nano Lett. 2008. **8**: pp. 3475-3480.

[166]- G. Koblmuller, S. Hertenberger, K. Vizbaras, M. Bichler, F. Bao, J.P. Zhang, and G. Abstreiter, *Self-induced growth of vertical free-standing InAs nanowires on Si(111) by molecular beam epitaxy.* Nanotechnology, 2010. **21**: pp. 365602.

[167]- P. Caroff, M.E. Messing, B. Mattias Borg, K.A. Dick, K. Deppert, and L.E. Wernersson, *InSb heterostructure nanowires: MOVPE growth under extreme lattice mismatch.* Nanotechnology, 2009. **20**: pp. 495606.

[168]- L. Lugani, D. Ercolani, F. Rossi, G. Salviati, F. Beltram, and L. Sorba, *Faceting of InAs–InSb Heterostructured Nanowires.* Cryst. Growth Des. 2010. **10**: pp. 4038-4042.

[169]- X. Weng, R.A. Burke, E.C. Dickey, and J.M. Redwing, *Effect of reactor pressure on catalyst composition and growth of GaSb nanowires.* J. Cryst. Growth. 2010. **312**: pp. 514-519.

[170]- L.G. Wang, P. Kratzer, N. Moll, and M. Scheffler, *Size, shape, and stability of InAs quantum dots on the GaAs(001) substrate.* Phys. Rev. B. 2000. **62**: pp. 1897-1904.

[171]- J. Xiang, W. Lu, Y.J. Hu, Y. Wu, H. Yan, and C.M. Lieber, *Ge/Si nanowire heterostructures as high-performance field-effect transistors.* Nature, 2006. **441**: pp. 489-493.

[172]- L.J. Lauhon, M.S. Gudiksen, C.L. Wang, and C.M. Lieber, *Epitaxial core-shell and core-multishell nanowire heterostructures.* Nature, 2002. **420**: pp. 57-61.

[173]- M. Heurlin, O. Hultin, K. Storm, D. Lindgren, M.T. Borgstrom, and L. Samuelson, *Synthesis of Doped InP Core-Shell Nanowires Evaluated Using Hall Effect Measurements.* Nano Lett. 2014. **14**: pp. 749-753.

[174]- G. Mariani, Z. Zhou, A. Scofield, and D.L. Huffaker, *Direct-bandgap epitaxial core-multishell nanopillar photovoltaics featuring subwavelength optical concentrators.* Nano Lett. 2013. **13**: pp. 1632-1637.

[175]- K. Kawaguchi, M. Heurlin, D. Lindgren, M.T. Borgström, M. Ek, and L. Samuelson, *InAs quantum dots and quantum wells grown on stacking-fault controlled InP nanowires with wurtzite crystal structure.* Appl. Phys. Lett. 2011. **99**: pp. 131915.

[176]- H. Asai, *Anisotropic lateral growth in GaAs MOCVD layers on (001) substrates.* J. Cryst. Growth. 1987. **80**: pp. 425-433.

[177]- Y.-N. Guo, H.-Y. Xu, G.J. Auchterlonie, T. Burgess, H.J. Joyce, Q. Gao, H.H. Tan, C. Jagadish, H.-B. Shu, X.-S. Chen, W. Lu, Y. Kim, and J. Zou, *Phase Separation Induced by Au Catalysts in Ternary InGaAs Nanowires.* Nano Lett. 2013. **13**: pp. 643-650.

[178]- P.K. Mohseni, A. Behnam, J.D. Wood, C.D. English, J.W. Lyding, E. Pop, and X. Li, *In$_x$Ga$_{1-x}$As nanowire growth on graphene: van der Waals epitaxy induced phase segregation.* Nano Lett. 2013. **13**: pp. 1153-1161.

[179]- A. Fakhr, Y.M. Haddara, and R.R. Lapierre, *Dependence of InGaP nanowire morphology and structure on molecular beam epitaxy growth conditions.* Nanotechnology, 2010. **21**: pp. 165601.

[180]- Y. Kim, H.J. Joyce, O. Gao, H.H. Tan, C. Jagadish, M. Paladugu, J. Zou, and A.A. Suvorova, *Influence of nanowire density on the shape and optical properties of ternary InGaAs nanowires.* Nano Lett. 2006. **6**: pp. 599-604.

[181]- M.T. Borgström, J. Wallentin, K. Kawaguchi, L. Samuelson, and K. Deppert, *Dynamics of extremely anisotropic etching of InP nanowires by HCl.* Chem. Phys. Lett. 2011. **502**: pp. 222-224.

[182]- A. Berg, S. Lehmann, N. Vainorius, A. Gustafsson, M.-E. Pistol, L.R. Wallenberg, L. Samuelson, and M.T. Borgström, *Growth and characterization of wurtzite GaP nanowires with control over axial and radial growth by use of HCl in-situ etching.* J. Cryst. Growth. 2014. **386**: pp. 47-51.

[183]- D. Jacobsson, J.M. Persson, D. Kriegner, T. Etzelstorfer, J. Wallentin, J.B. Wagner, J. Stangl, L. Samuelson, K. Deppert, and M.T. Borgstrom, *Particle-assisted Ga$_x$In$_{1-x}$P nanowire growth for designed bandgap structures.* Nanotechnology, 2012. **23**: pp. 245601.

[184]- I. Regolin, V. Khorenko, W. Prost, F.J. Tegude, D. Sudfeld, J. Kästner, and G. Dumpich, *Composition control in metal-organic vapor-phase epitaxy grown InGaAs nanowhiskers.* J. Appl. Phys. 2006. **100**: pp. 074321.

[185]- C.S. Jung, H.S. Kim, G.B. Jung, K.J. Gong, Y.J. Cho, S.Y. Jang, C.H. Kim, C.-W. Lee, and J. Park, *Composition and Phase Tuned InGaAs Alloy Nanowires.* J. Phys. Chem. C. 2011. **115**: pp. 7843-7850.

[186]- J.A. McCaulley, *Kinetics of thermal decomposition of triethylgallium, trimethylgallium, and trimethylindium adsorbed on GaAs(100).* J. Vac. Sci. Technol. A. 1991. **9**: pp. 2872-2886.

9. Acknowledgements

Many people have helped me a great deal on my PhD journey. First of all, I would like to thank my main supervisor Dr. Kimberly A. Dick. You have always inspired me with your incredible knowledge and skills in nanowire growth and it has been an honor to work with you. Thank you for always finding time for me, for all the discussions about crystal growth, TEM, and just anything.

I would like to thank my excellent assistant supervisors Prof. Knut Deppert and Dr. Jonas Johansson. Thank you Knut for being such a supportive and caring supervisor and for helping me to find my way. Thank you Jonas for all the support, scientific discussions and the conference trips we took together.

I would also like to thank Prof. Lars-Erik Wernersson for giving me the opportunity to come to Lund and work in this exciting field, and for all the scientific discussions we had together.

Dr. Erik Lind is gratefully acknowledged for teaching me many interesting things about the physics of devices.

I gratefully acknowledge Dr. Philippe Caroff. Your enthusiasm for research has always motivated me. Thank you for the excellent collaboration on the GaInSb project and for finding time to read my long e-mails and manuscripts, even when on vacation.

Dr. Martin Ek is gratefully acknowledged for his excellent TEM work. Thank you Martin for all the time you spent looking at the antimonide nanowires, and also for teaching me a lot about TEM.

Dr. Sebastian Lehmann, you taught me to think about all the important details both in experiments and manuscripts. Thank you for all the scientific discussions we had together and for your valuable comments on part of this thesis.

Prof. Reine Wallenberg and Dr. Crispin Hetherington are also acknowledged for teaching me how TEM works.

During my PhD study, I had the opportunity to spend some time at NTNU in Trondheim. Therefore, I would like to thank Prof. Helge Weman, Prof. Bjørn-Ove Fimland, Dr. Dasa. L Dheeraj, and A. Mazid Munshi for welcoming me there and teaching me everything I know about MBE. Thank you Dheeraj for helping me to get started there, and thank you Mazid for all the discussions we had together while growing our samples.